applied sciences

MDPI

Article

Numerical Simulation of Shock Wave Generation and Energy Conversion Efficiency in Underwater Nanosecond Pulsed Discharge

Jiaqi Deng [1], Kehan Cao [1], Huapeng Li [1], Yanqun Fu [2], Chao Lyu [2], Yunpeng Lu [2], Qiang Yue [2], Mingyi Zhang [2], Jiaqi Wen [2], Peng Wang [2], Zhiyuan Ma [2], Zongyu Liu [2] and Baipeng Song [1,*]

[1] School of Electrical Engineering, Xi'an Jiaotong University, Xi'an 710049, China
[2] HCIG Engineering & Construction Co., Ltd., Shijiazhuang 050051, China
* Correspondence: bpsong@xjtu.edu.cn

Abstract

Shock waves generated by underwater nanosecond pulsed discharge offer advantages such as high peak pressure, broad bandwidth, and strong controllability, showing promising application prospects in areas like underwater acoustic sources. Current research largely focuses on individual stages and lacks a full-process analysis framework that spans from discharge parameters to shock wave output. To address this, this paper develops a numerical simulation model covering both the pre-breakdown and main discharge stages. In the pre-breakdown stage, based on field-induced ionization theory, coupled equations of charged particle drift-diffusion, Poisson's equation, and heat transfer are established to simulate the evolution of the streamer from initiation to bridging; the parameters obtained at the end of pre-breakdown are then used as initial values for the main discharge stage. In the main discharge stage, the plasma channel is modeled as a variable-resistance cylinder, and the discharge circuit is coupled with the energy conservation equation to quantitatively describe the conversion process from electrical energy to the mechanical energy of the shock wave, as well as to analyze the attenuation characteristics of the shock wave during near-field propagation. Based on the above, this paper systematically investigates the influence of pulse voltage amplitude, electrode gap, and electrode curvature radius on the discharge process and energy conversion. Increasing the voltage can shorten the breakdown time delay and enhance the deposited energy, but high-temperature radiation leads to a decrease in the shock wave energy conversion efficiency; increasing the electrode gap distance is beneficial for enhancing the deposited energy, but increases thermal radiation loss; increasing the curvature radius has a limited effect on improving energy conversion. The influence of each parameter on the shock wave amplitude exhibits a saturation effect, the intrinsic mechanism of which stems from the competition between the deposited energy gain and the dissipation mechanism. The integrated simulation framework established in this paper provides a basis for analysing parameter trends and for guiding the design of underwater pulsed discharge acoustic sources, subject to the assumptions and validation discussed in the paper.

Keywords: pulse discharge in water; shock wave; nanosecond pulsed discharge; pre-breakdown; arc detonation; streamer morphology; energy conversion efficiency

Academic Editor: Michel Darmon

Received: 12 September 2026
Revised: 26 October 2026
Accepted: 6 November 2026
Published: 12 November 2026

Copyright: © 2026 by the authors. Licensee MDPI, Basel, Switzerland. This article is an open access article distributed under the terms and conditions of the Creative Commons Attribution (CC BY) license.

1. Introduction

Underwater high-voltage pulsed discharge can convert electrical energy into mechanical energy, light energy, and thermal energy within a short period of time. Underwater shock waves are also generated by explosive charges [1], while laser-driven optoacoustic sources provide a contact-free alternative for pulsed acoustic excitation [2]. Compared with these methods, underwater pulsed discharge is capable of producing a higher pulse sound pressure level and offers advantages such as compact size, broad frequency bandwidth, high repetition rate, and controllable emission mode; it has also been examined as a non-lethal swimmer deterrent [3]. In addition, the water medium can significantly enhance the peak pressure, impulse, and energy of the shock wave, while the discharge is accompanied by bubble cavitation and high-speed jet effects [4]. This phenomenon, known as the electrohydraulic effect, involves the formation of a penetrating high-temperature plasma channel in water under a high-voltage pulse; the immense temperature and pressure difference between the interior and exterior of the channel drives its rapid expansion and outward radiation of shock waves [5,6]. Shock waves generated by underwater pulsed discharge exhibit significant advantages in terms of acoustic characteristics and application scope. Therefore, an in-depth understanding of the mechanism of underwater high-voltage pulsed discharge, investigation of the influences of various factors on water breakdown characteristics and shock wave generation modes, establishment of a comprehensive electro-acoustic conversion model, and exploration of the focusing effect of directional radiation technology are of great significance for studying the mechanisms and applications of underwater pulsed discharge shock waves [7,8].

Under high-voltage pulses, the breakdown of water is divided into two major stages: the pre-breakdown stage and the main discharge stage. The pre-breakdown process mainly involves the generation and evolution of streamers, which are constrained by multiple factors such as water conductivity, electrode geometry, and pulse rise time [9,10]. After the streamer fully bridges the electrodes, the main discharge stage begins. Currently, three mature theories exist in the academic community regarding the initiation mechanism of streamers: the bubble discharge theory, the field-induced ionization theory, and the electrostriction theory, each applicable to different scenarios and physical processes [11].

The bubble discharge theory applies to microsecond-scale pulses. Joule heating at the electrode tip generates microbubbles, which provide the mean free path for electron-avalanche collisional ionization [12,13]. However, bubble formation relies on thermal accumulation and requires hundreds of nanoseconds, making it unsuitable for nanosecond fast-rise-time pulses [14,15].

The field-induced ionization theory is commonly used to describe water breakdown under nanosecond and picosecond ultrashort pulses. In this case, no pre-existing bubbles are present; instead, the strong electric field directly tears water molecules apart, producing electrons and positive ions, forming a space-charge region that drives streamer propagation [16]. This theory extends the solid-state Zener tunneling ionization to liquid water and gives the relationship between the field-ionization rate, electric field strength, and molecular number density [17].

The electrostriction theory points out that the non-uniform strong electric field at the electrode tip generates electrostrictive forces. When these forces exceed a critical value of about 24 MPa, nanoscale vacuum cavities are created [18]. The abrupt dielectric change at the cavity interface enhances the local electric field, leading to field-induced ionization of water molecules at the cavity walls. Electrons then multiply inside the cavity via acceleration and trigger streamer development. The essence of cavity breakdown is still based on field-induced ionization [19,20].

https://doi.org/10.3390/app162211229

By comprehensively comparing the applicability conditions and physical fundamentals of these three theories, this work ultimately selects the field-induced ionization theory for numerical simulation of the pre-breakdown process under nanosecond pulses [21].

The shock wave generated by underwater pulsed discharge undergoes three stages: arc expansion, shock wave propagation, and bubble pulsation [22,23]. The pulsed discharge creates a high-temperature, high-pressure plasma channel. As the channel expands, it vaporizes the surrounding water to form an initial bubble. The expansion of this bubble compresses the surrounding water medium, thereby generating a shock wave [24]. When the bubble expands to the point where its internal pressure falls below the ambient water pressure, it begins to collapse. Upon collapse, when the internal pressure again exceeds the water pressure, it re-expands. This repeated expansion-collapse process constitutes the bubble pulsation. The collapse and destruction of the bubble radiate a secondary pressure wave with lower energy but longer duration, and the final collapse produces a high-speed microjet [25].

Experiments have revealed that in the near field, the shock wave behaves as a cylindrical wave, whereas in the far field it transitions to a spherical wave; the attenuation rates of these two regimes differ considerably [26]. The initial wave velocity can reach as high as 3.5 km/s, followed by a rapid decay to approximately 1.5 km/s [27]. The shock wave energy and peak pressure exhibit a trend of first increasing and then decreasing with variations in the discharge gap. The peak pressure of the shock wave is positively correlated with the breakdown voltage and the discharge current [28]. An increase in deposited energy can enhance the shock wave intensity; however, energy losses due to high-temperature radiation introduce a saturation effect [29].

Recent studies can be grouped by the stage of the discharge that they resolve. On the pre-breakdown side, drift–diffusion and multiphysics models reproduce field-induced ionization, space-charge distortion and streamer inception and propagation in water under nanosecond pulses, and quantify how the voltage amplitude, gap distance and pulse rise time change the streamer field and electron density [14,15,19,20,30,31]; these models, however, terminate at the streamer stage and do not carry the computed channel state into the main discharge. On the main-discharge side, arc-detonation, channel-expansion and spark-resistance models describe the expanding channel, the pressure wave and its attenuation, using a time-varying channel resistance, an isothermal channel model or a tabulated equation of state and conductivity [23,32–35]. Even the most recent of these models couples the circuit, the channel thermodynamics and the pressure wave, yet prescribes the initial channel temperature, current, density and radius, and accounts for the preceding stage only as a fraction of the stored energy lost to form the streamer [34]; the two stages are therefore still linked by an assumed energy partition rather than by a computed terminal streamer state. Experimental studies quantify the peak pressure, impulse, attenuation and electro-acoustic efficiency over ranges of voltage, gap and tip curvature [4–6,21,25,29,36,37]; they show that the breakdown delay and the deposited energy control the output, but they do not resolve how the energy expended before breakdown and the terminal streamer geometry set the energy available to the shock wave. Consequently, the fraction of the stored electrical energy that reaches the near-field shock wave has not been evaluated within a single parameter-consistent framework, and this is the gap addressed in the present work.

This paper establishes a complete simulation framework from pre-breakdown to shock wave generation for nanosecond pulsed discharge in water. The individual submodels are adopted from previous work; what is new is their sequential coupling, through which the computed terminal streamer state initializes the arc-detonation model, and the energy accounting that this coupling makes possible. It combines a field-induced

ionization pre-breakdown model with an arc detonation main-discharge model, and analyzes the effects of voltage amplitude, electrode gap, and electrode curvature on discharge characteristics and energy conversion efficiency to support underwater directional acoustic energy device optimization.

2. Modelling Setup

The preceding sections have reviewed the mechanisms of pulsed discharge in water and the current state of research on shock wave generation and propagation, identifying the deficiency of a lack of an integrated analytical framework covering the entire process. To enable a complete simulation from the input of discharge parameters to shock wave propagation, this chapter elaborates on the theoretical models and numerical methods: the field-induced ionization theory is adopted to establish a multiphysics coupling model for pre-breakdown, an arc detonation model for the main-discharge stage and the governing equations for shock wave propagation are constructed, and the electrode geometry and boundary conditions for the pre-breakdown simulation are provided by COMSOL Multiphysics 6.3. The effects of pulse voltage amplitude, electrode gap, and curvature radius on the pre-breakdown streamer and the energy conversion in the main discharge are investigated by setting multiple sets of variables while keeping other model boundary conditions unchanged; details are given in the Results section below. The overall workflow of the coupled simulation is summarized in Figure 1. Input parameters are passed to the COMSOL pre-breakdown model; the terminal streamer state is used as the initial condition of the MATLAB R2025a main-discharge model, which yields the shock pressure and the energy conversion efficiencies.

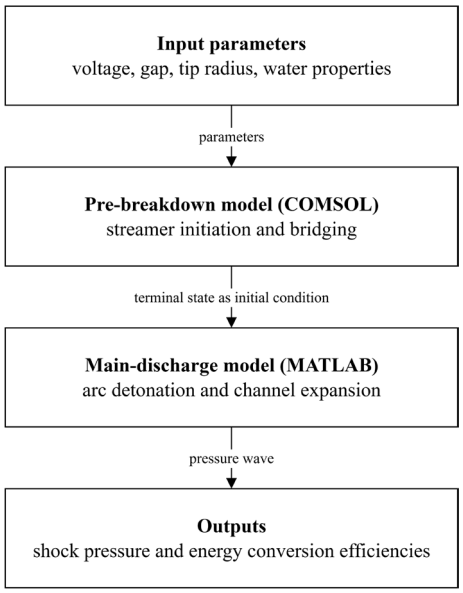


Figure 1. Workflow of the coupled simulation.

The individual submodels used in this section are not new, and no priority is claimed for them. The field-ionization source term of Equation (1) is the Zener-tunnelling form applied to liquid water [16,17]; the drift–diffusion system of Equations (2)–(4) and its transport coefficients follow Ref. [30]; Equations (5)–(7) are the standard Poisson and Joule-heating formulations; and the channel model of Equations (8)–(13), comprising the temperature-dependent conductivity and resistance, the lumped circuit, the Braginskii–Martin energy balance and the Tait/Rankine-Hugoniot pressure–velocity relation, follows Refs. [32,33]. What is new in this work is the way in which these components are linked: the terminal streamer state computed by the COMSOL pre-breakdown model—channel

radius, length, temperature and particle density—is passed directly to the MATLAB arc-detonation model as its initial condition, so that the main-discharge calculation starts from a computed channel state rather than from a prescribed channel radius, temperature or energy-partition coefficient [34]. The same coupling is then exercised over a common sweep of voltage amplitude, electrode gap and tip curvature, so that each parameter acts on the shock wave both through the breakdown delay and through the channel state that it produces. Finally, the coupled solution is used to separate the deposited-energy efficiency from the shock-wave energy efficiency and to analyze their opposite trends and the resulting saturation of the peak pressure, which cannot be obtained from either stage alone.

2.1. Discharge Pre-Breakdown Model

Both the field-induced ionization theory and the electrostriction theory can describe the initiation of nanosecond pulsed discharge in water. However, since the cavity-wall breakdown in the electrostriction theory essentially relies on field-induced ionization, this work adopts the field-induced molecular ionization theory, with field-induced ionization serving as the primary mechanism for the ionization source term. The applied high-voltage electric field ionizes water molecules, generating positive ions and electrons. The electrons attach to water molecules to form negative ions, leading to local charge accumulation and the generation of a space-distorted electric field. Driven jointly by the external electric field, the distorted electric field, and concentration gradients, the charged particles develop streamers through drift-diffusion processes, eventually bridging the electrodes and completing the pre-breakdown. This process is accompanied by complex phenomena such as charged-particle attachment, recombination, and energy transfer, which collectively govern the dynamic behavior of the streamers.

Under the field-induced ionization theory, water molecules are ionized by the applied electric field, producing positive ions and electrons. According to the Zener tunneling theory, the generation rates of positive ions and electrons can be calculated as follows:

$$G_1\left(\left|\vec{E}\right|\right)=\frac{en_0\left|\vec{E}\right|a}{h}\exp\left(-\frac{m_e a\pi^2\Delta^2}{e\left|\vec{E}\right|h^2}\right) \quad (1)$$

In the above equations, n_0 is the ionizable molecular number density of water; a is the molecular spacing of water; h is Planck's constant; m_e is the effective electron mass; and Δ is the ionization energy of water molecules, that is, the energy required to ionize a water molecule into a positive ion and an electron.

The interactions among charged particles are primarily described through two mechanisms: recombination and attachment. Recombination refers to the process in which positive ions combine with negative ions or electrons to form neutral particles, and the corresponding recombination rate coefficients are denoted as β_{pn} and β_{ep}, respectively. Attachment refers to the process in which electrons attach to water molecules to form negative ions, which is expressed using the attachment time constant (denoted as τ or its equivalent in the specific formulation). Let n_p, n_n, and n_e represent the number densities of positive ions, negative ions, and electrons, respectively, and D_p, D_n, D_e be their corresponding diffusion coefficients. By comprehensively considering the drift motion under the electric field, diffusion driven by concentration gradients, and the aforementioned reaction processes, the continuity equations describing the evolution of the number densities of each charged species can be established [30], whose general form is given as follows:

$$\frac{\delta n_p}{\delta t}+\nabla\bullet\left(n_p\mu_p\vec{E}\right)-D_p\nabla^2 n_p=G_1\left(\left|\vec{E}\right|\right)-\frac{n_p n_n\beta_{pn}}{e}-\frac{n_p n_e\beta_{ep}}{e} \tag{2}$$

$$\frac{\delta n_n}{\delta t}-\nabla\bullet\left(n_n\mu_n\vec{E}\right)-D_n\nabla^2 n_n=\frac{n_e}{\tau}-\frac{n_p n_n\beta_{pn}}{e} \tag{3}$$

$$\frac{\delta n_e}{\delta t}-\nabla\bullet\left(n_e\mu_e\vec{E}\right)-D_e\nabla^2 n_e=G_1\left(\left|\vec{E}\right|\right)-\frac{n_p n_e\beta_{ep}}{e}-\frac{n_e}{\tau} \tag{4}$$

In the above equations, the terms $\delta n_p/\delta t$, $\delta n_n/\delta t$ and $\delta n_e/\delta t$ represent the rates of change of the number densities of positive ions, negative ions and electrons, respectively; the terms $\nabla\cdot(n_p\mu_p\vec{E})-D_p\nabla^2 n_p$, $-\nabla\cdot(n_n\mu_n\vec{E})-D_n\nabla^2 n_n$ and $-\nabla\cdot(n_e\mu_e\vec{E})-D_e\nabla^2 n_e$ denote the divergences of the respective particle fluxes, which characterize the drift–diffusion processes of the charged species; the terms $n_p n_n\beta_{pn}/e$ and $n_p n_e\beta_{ep}/e$ are the recombination terms for positive ions with negative ions and with electrons, respectively; and the term n_e/τ corresponds to the attachment of electrons to water molecules.

To account for the feedback effect of space charge on the electric field, the Poisson equation is introduced, which directly relates the electric field to the space charge density:

$$\nabla\bullet\left(\varepsilon_0\varepsilon_r\vec{E}\right)=n_p+n_n+n_e \tag{5}$$

In the equation, $\vec{E}$ denotes the spatial distribution of the electric field. By solving the Poisson equation together with the particle transport equations, a self-consistent coupling between the charge distribution and the electric field evolution is achieved, thereby capturing the electric field enhancement at the streamer head and its propagation process.

During the pre-discharge stage, the motion of charged particles gives rise to a conduction current, which in turn generates Joule heating that raises the temperature of the water. To quantitatively describe this electro-thermal coupling process, a Joule heat source term is introduced into the conventional heat transfer differential equation, thus establishing the heat transfer governing equation applicable to discharges in water:

$$\rho C_p\frac{\partial T}{\partial t}=k\nabla^2 T+Q_e \tag{6}$$

In the equation, ρ denotes the density of water. Since the density of water varies significantly with temperature, it is treated as a function of temperature in the simulation to improve the model's accuracy in describing transient thermal processes, with its initial value set to that corresponding to the normal temperature of 293.15 K. C_p represents the specific heat capacity of water, and k is the thermal conductivity of water; both are key physical property parameters that influence energy transfer and temperature distribution. Q_e denotes the Joule heat source term arising from the conduction current, reflecting the conversion of electrical energy into thermal energy, the specific expression of which is given by Equation (7):

$$Q_e=\vec{E}\cdot\vec{J} \tag{7}$$

where $\vec{J}$ is the conduction current density. Through the above heat transfer model, the temperature distribution and its temporal evolution during the streamer development process can be calculated, providing the initial temperature conditions for the subsequent main-discharge stage.

The geometric model of the needle-plate electrode configuration established in this work is shown in Figure 2, where the radius of curvature of the needle tip is set to 0.25

mm, and the needle-plate gap is set to 2 mm. Owing to the axisymmetric nature of this electrode structure, and because the development range of the streamer during the pre-breakdown process typically does not exceed the radial extent of the needle electrode, a 2D axisymmetric model is adopted on the right side of the needle axis as the computational domain to reduce the computational cost.

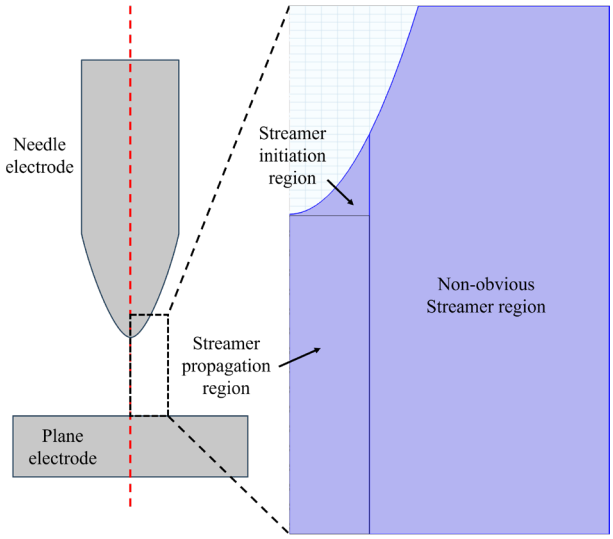


Figure 2. Needle-Plate Electrode Geometry Model.

The pre-breakdown model is solved in a two-dimensional axisymmetric domain with the needle–plate geometry of Figure 2. The applied pulse is $V_{app}(t) = 200(e^{-t/730} - e^{-t/70})$ kV, which peaks at 141 kV. The needle electrode is held at $V_{app}(t)$, the plate electrode is grounded, and the needle axis is treated as a symmetry boundary. The species densities are set to 1×10^{12} m^{-3} at both electrodes and as initial values throughout the domain, and the outer boundary is an open boundary with a convective heat flux of 500 $W \cdot m^{-2} \cdot K^{-1}$. The domain is meshed with a mapped mesh of 400 divisions along the channel axis and 100 elements in the radial direction with a growth ratio of 1.5, free triangular elements with a maximum size of 5 μm, and five boundary layers with a stretching ratio of 1.5. The transient solver uses the BDF method with a relative tolerance of 0.01, an absolute-tolerance factor of 0.1, a maximum time step of min (0.1 ns, $0.8\tau_{DRT}$), where τ_{DRT} is the minimum dielectric relaxation time of the discharge model, and an output interval of 0.1 ns.

2.2. Main-Discharge Arc Detonation Model

When the streamer formed during the pre-breakdown stage fully bridges the two electrodes, the pre-breakdown process ends, and the system enters the main discharge stage, as illustrated in Figure 3. At this stage, the power supply energy is injected into the plasma channel within an extremely short time, triggering intense energy conversion: part of the energy is converted into internal energy, causing a sharp rise in temperature and pressure; another part is converted into mechanical energy, driving the channel to expand rapidly and pushing the surrounding water medium into motion.

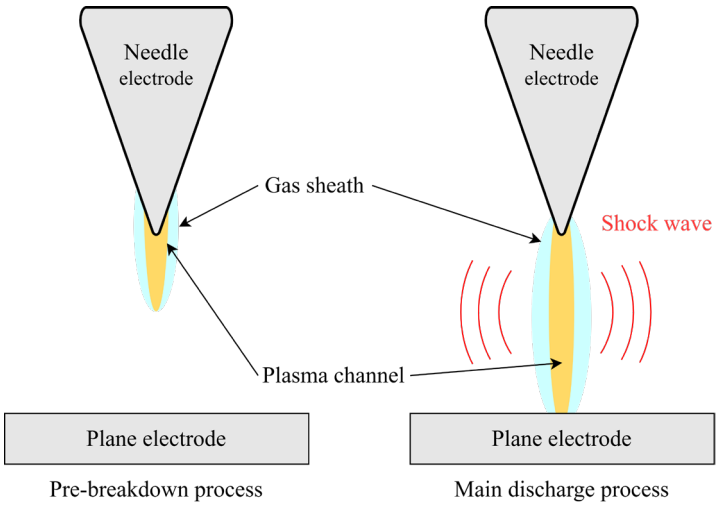


Figure 3. Schematic of the transition from pre-breakdown to main discharge.

Meanwhile, through radiative heat transfer and thermal conduction, the surrounding water is rapidly heated, vaporized, and ionized, becoming part of the plasma and promoting continuous channel expansion. The low compressibility of water causes the rapid channel expansion to generate a strong impact pressure in the surrounding liquid, thereby exciting a high-intensity shock wave. This shock wave, characterized by high peak pressure and fast propagation speed, is the primary source of the acoustic and mechanical effects generated by pulsed discharge in water.

After the streamer formed in the pre-breakdown stage fully bridges two electrodes, the discharge channel can be approximately regarded as a cylindrical plasma region. Based on this geometric simplification, the discharge channel is modeled as a cylinder, and the equivalent resistance of the channel in the discharge circuit is calculated accordingly, as shown in Equation (8):

$$R_p = \frac{l}{\pi a^2 \sigma_p} \tag{8}$$

where l is the length of the plasma channel, a is the radius of the plasma channel, and σ_p is the electrical conductivity of the discharge channel, which is a function of temperature and can be calculated using the empirical formula for plasma conductivity given in Equation (9):

$$\sigma_p = \xi \cdot (kT)^{3/2} \tag{9}$$

where ξ is the conductivity coefficient, with a value of 5.4×10^{31} $S \cdot J^{-3/2} \cdot m^{-1}$; k is the Boltzmann constant; and T is the temperature in kelvin.

During the main discharge stage, the electrical energy stored in the capacitor is rapidly released through the external circuit into the discharge gap, forming a high-energy pulsed discharge. To quantitatively describe the current, voltage, and energy transfer characteristics during this process, the actual discharge system can be abstracted as a lumped-parameter equivalent circuit. This circuit includes the storage capacitor C, the circuit inductance L, the circuit resistance R_{cir}, and the time-varying resistance R_p that characterizes the dynamic behavior of the discharge gap. This equivalent circuit can comprehensively reflect the electrical characteristics of the discharge loop and its interaction with the plasma channel. Based on this equivalent circuit, the corresponding discharge loop equations can be formulated as follows:

$$U_C = R_{cir} \cdot I + R_p \cdot I + L \cdot \frac{dI}{dt} \tag{10}$$

where C = 20 nF, L = 2.555 μH and R_{cir} = 4 Ω. For the 140 kV case, the capacitor is charged to U_0 = 165 kV, so that the stored energy is $E_0 = CU_0^2/2$ = 272.25 J; in the voltage sweep, the charging voltage scales with the gap voltage.

$$\begin{cases} U_p = R_p \cdot I \\ U_C = Q/C \\ I = -dQ/dt \end{cases} \tag{11}$$

where U_C is the voltage across the capacitor, U_P is the voltage across the discharge channel, and Q is the charge stored in the capacitor. By solving the above equations, the temporal evolution of the current during the main discharge stage can be obtained.

Once the main discharge stage commences, the electrical energy stored in the capacitor is rapidly released and converted into multiple energy forms through electro-thermal-mechanical coupling, mainly including: the internal energy of the discharge channel, the mechanical energy driving the shock wave, and the energy dissipated to the surrounding medium via thermal radiation and thermal conduction. To quantitatively describe this energy conversion process, the energy conversion equation for the main discharge stage is established based on the Braginskii–Martin model as follows:

$$p\frac{dV}{dt} + \frac{d(WV)}{dt} + S\sigma_S T^4 = I^2 R_p \tag{12}$$

where p is the pressure of the plasma channel; W is the internal energy per unit volume within the channel; σ_S is the Stefan–Boltzmann radiation constant, with a value of 5.67 × 10^{-8} W/(m²·K⁴). The first term on the left-hand side represents the mechanical power performed by the channel on the surrounding water medium during expansion, the second term denotes the rate of change of the internal energy of the channel, and the third term corresponds to the radiative heat loss at the channel boundary; the right-hand side represents the net power input into the channel through Joule heating.

After approximating the plasma channel as a cylindrical model, the relationship between the channel radius expansion velocity and the channel wall pressure can be established based on the Rankine–Hugoniot shock conditions:

$$\frac{da}{dt} = \left(\frac{\sqrt{7}\alpha^{1/14}}{3\sqrt{\rho_0}} \right) \left[(p+\beta)^{3/7} - \beta^{3/7} \right] \tag{13}$$

where ρ_0 is the density of water, taken as 1000 kg/m³. The coefficients α and β are the constants of the Tait equation of state of water adopted in this work, $p + \beta = \alpha(\rho/\rho_0)^7$, rather than empirically adjusted shock coefficients: n = 7 is the Tait exponent for water, β = 300 MPa is the Tait pressure constant, and $\alpha = \beta + p_0$ = 300.1 MPa is fixed by the condition that the overpressure vanishes at $\rho = \rho_0$, where $p_0 \approx 0.1$ MPa is the ambient pressure. Equation (13) is derived in Ref. [33] by combining this equation of state with the Rankine–Hugoniot conditions applied to the expanding channel wall; it is used here to couple the channel pressure to the expansion velocity and to provide the initial condition for the shock wave propagation model. In the limit $p \ll \beta$, Equation (13) reduces to the acoustic relation $u = p/(\rho_0 c_0)$ with $c_0 = (7\alpha/\rho_0)^{1/2} \approx 1.45$ km/s, i.e., the sound speed of water given by the same equation of state. The particle number density inside the channel is not constant and evolves as:

$$\frac{dn}{dt} = \frac{2}{a}\left(\frac{\sigma_S T^4}{\varepsilon_{\text{vap}}} - n\frac{da}{dt}\right) \tag{14}$$

The pressure at a distance r from the channel is obtained by representing the channel as an equivalent sphere of radius $a_s = (3a^2l/4)^{1/3}$ and scaling the channel pressure by geometric spreading:

$$p_w(t_r) = \max\left\{0, \frac{a_s\, p(t)}{r} - p_{\text{amb}}\right\} \tag{15}$$

where $t_r = t + (r/c_0)$, $c_0 = 1500$ m·s^{-1} and $p_{amb} = 101{,}325$ Pa. This relation accounts for the spherical spreading of the wave and for the acoustic propagation delay; it does not resolve the viscous and thermal structure of the shock front, so the attenuation of the peak pressure with distance is attributed to geometric spreading and to the decay of the source pressure rather than to a modelled dissipation term. The stored, deposited and shock-wave energies are $E_0 = CU_0^2/2$, $E_{dep} = \int I^2 R_p\, dt$ and $E_{sw} = (4\pi r^2/\rho_0 c_0) \int p_w^2\, dt$, and the corresponding efficiencies are:

$$\begin{cases} \eta_B = \dfrac{E_{\text{dep}}}{E_0} \\ \eta_E = \dfrac{E_{\text{sw}}}{E_{\text{dep}}} \\ \eta = \dfrac{E_{\text{sw}}}{E_0} \end{cases} \tag{16}$$

2.3. Model Assumptions and Limitations

Table 1 consolidates the parameters used in the two stages, together with their values or ranges and their sources. Parameters given as ranges are those varied in Section 3.3; all remaining quantities are fixed at the values listed.

Table 1. Parameters of the two-stage discharge model.

Symbol	Definition	Value or Range	Source
U_{gap}	Peak voltage at the gap	70–140 kV	Section 3.1, Section 3.3.1
t_r	Rise time	90 ns	Section 3.1
d	Needle–plate gap	1–5 mm (baseline 2 mm)	Section 3.3.2
r_c	Tip curvature radius	0.1–0.4 mm (baseline 0.25 mm)	Section 3.3.3
T_w	Initial water temperature	293.15 K	Section 2.1
ε_r	Relative permittivity	83	model input
ε_0	Vacuum permittivity	8.85×10^{-12} F·m^{-1}	model input
n_0	Ionizable molecule density	3.3×10^{24} m^{-3}	model input
a	Molecular spacing	0.31 nm	model input
m_e	Effective electron mass	9.1×10^{-32} kg	model input
Δ	Ionization energy	4 eV	model input
λ_e	Electron attenuation length	1 mm	model input
μ_p, μ_n, μ_e	Mobilities	1×10^{-6}, 1×10^{-6}, 3×10^{-2} m^2·V^{-1}·s^{-1}	model input
β_{pn}, β_{ep}, τ	Recombination and attachment coefficients	1×10^{-19} m^3·s^{-1}, 1×10^{-19} m^3·s^{-1}, 200 ns	model input
C	Capacitance	20 nF	model input
L	Inductance	2.555 μH	model input
R_{cir}	Circuit resistance	4 Ω	model input

U_0	Charging voltage	165 kV at 140 kV gap voltage	model input
E_0	Stored energy	272.25 J	derived
$a_{ch,0}$	Initial radius	0.05 mm	terminal streamer state
l	Channel length	2 mm	terminal streamer state
$T_{ch,0}$	Initial temperature	936 K	terminal streamer state
$n_{ch,0}$	Initial particle density	2.7737×10^{23} m^{-3}	terminal streamer state
γ	Isentropic exponent	1.35	Equation (12)
ε_{vap}	Vaporization energy	2.54×10^{-20} J	Equation (14)
ξ	Conductivity coefficient	5.4×10^{31} S·m^{-1}·J$^{-3/2}$	Equation (9)
α, β	Tait constants	300.1 MPa, 300 MPa	Equation (13)
σ_S	Stefan–Boltzmann constant	5.67×10^{-8} W·m^{-2}·K^{-4}	Equation (12)
σ_w	Electrical conductivity	3 S·m^{-1}	model input
ρ_0, c_0, p_{amb}	Density, sound speed, ambient pressure	1000 kg·m^{-3}, 1500 m·s^{-1}, 101 325 Pa	Equation (13)

In the voltage sweep, the charging voltage scales with the gap voltage (165 kV at 140 kV); the terminal channel state ($a_{ch,0}$, $T_{ch,0}$, $n_{ch,0}$) is taken from the corresponding pre-breakdown solution. The coupled equations were integrated with the fourth-order Runge–Kutta method, a time step of 0.05 ns and an end time of 100 μs.

Four assumptions bound the quantitative accuracy of the predictions. Their influence is assessed here from the mechanism through which each enters the calculation.

(1) The two-dimensional axisymmetric approximation suppresses branching and requires the streamer to remain a single azimuthally uniform filament. Three-dimensional branching would divide the deposited energy among several branches, reduce the energy per unit channel length, and thus lower the channel temperature and the peak pressure; at the same time, additional branches provide parallel paths to the counter-electrode and shorten the bridging time. The breakdown delay computed here is therefore an upper bound, and the peak pressure an upper bound for a strongly branched discharge, while the two effects partly compensate in the deposited-energy efficiency.

(2) The channel is treated as a straight cylinder of uniform radius. A real channel is tortuous and non-uniform, so that for the same deposited energy its length and surface area are larger, radiative and conductive losses are higher, and the pressure is lower. This effect is systematic and is expected to make the computed pressure slightly high, whereas its influence on the deposited energy is partly compensated by the corresponding change in channel resistance and current.

(3) Field-induced ionization is taken as the sole initiation mechanism. Bubble- and electrostriction-assisted pathways [12,13,19,20] would initiate the discharge at lower field and earlier in time; where they operate, the computed breakdown delay is an upper bound. These alternative mechanisms also change the plasma composition and the energy consumed before bridging, and therefore shift the deposited-energy efficiency rather than only the delay.

(4) The conductivity correlation of Equation (9) and the channel-expansion relation of Equation (13) assume a high-temperature plasma in local equilibrium with a sharp channel boundary, and the vaporization–condensation process is not resolved. A model that includes evaporation and condensation shows that these processes slow the pressure decay and broaden the pulse [34]; neglecting them therefore makes the computed pressure fall too rapidly and tends to underestimate the impulse, whereas the latent heat of vaporization would reduce the channel temperature and the peak pressure. Electrodes are treated as ideal boundaries, so sheath voltage drops, electrode heating and erosion are not represented; a sheath drop reduces the effective voltage across the channel together with the deposited energy and pressure, while

metal vapour from erosion would raise the channel conductivity. These electrode effects are expected to be secondary compared with the voltage and gap dependence resolved in Section 3.3, but they limit the absolute accuracy of the predicted pressure.

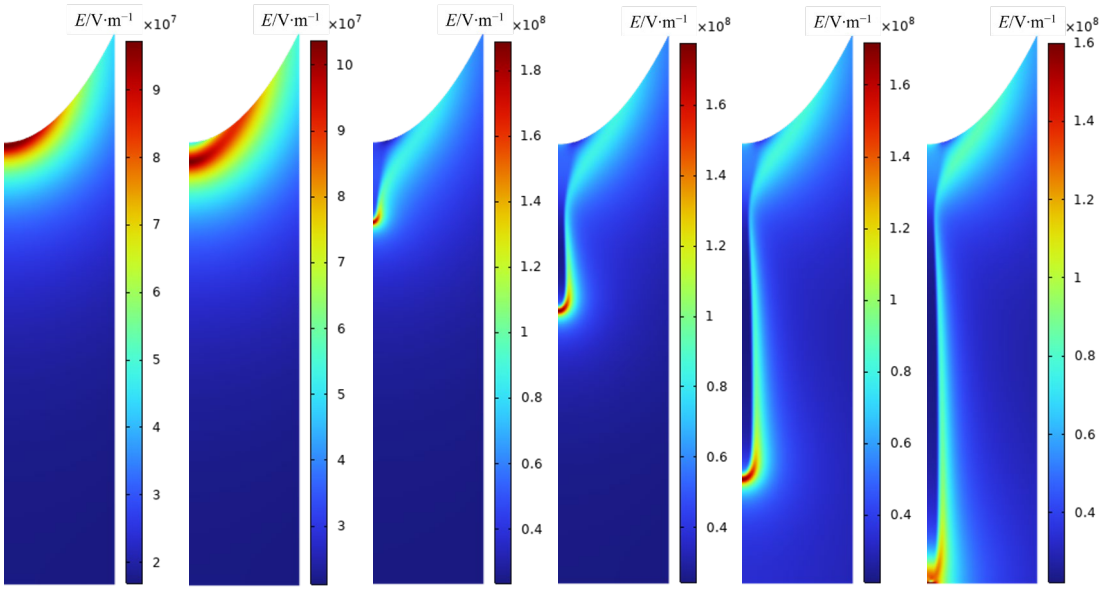
According to the above analysis, the key physical quantities within the discharge channel during the main discharge stage—including temperature, pressure, and particle number density—are closely coupled with one another. To comprehensively describe the dynamic evolution of the channel state, all the above governing equations must be solved simultaneously, thereby constructing an integrated model that systematically reflects the multiphysics characteristics of the discharge channel. For numerical solution, the fourth-order Runge–Kutta method is adopted to compute the strongly nonlinear, multi-variable coupled arc detonation model, balancing computational efficiency and accuracy.

3. Results & Discussion

In this chapter, the pre-breakdown model and the main-discharge model are applied to carry out simulation studies on the development process of discharges in water under nanosecond pulse voltage for the needle-plate electrode configuration. The investigation focuses on the morphological evolution of the streamer during the pre-breakdown process, as well as the arc channel characteristics and shock wave pressure waveforms during the main-discharge stage. To further explore the factors influencing discharge development, the pulse voltage amplitude, electrode gap, and electrode tip curvature radius are taken as the core variables, and the effects of each parameter on pre-breakdown streamer development and main-discharge energy conversion are examined through simulations.

3.1. Pre-Breakdown Process

In this section, a positive-polarity high-voltage pulse (peak voltage 140 kV, rise time 90 ns) is applied to the needle electrode, while the plate electrode is grounded. Based on the computational domain shown in Figure 2, the pre-breakdown process of water between the needle and plate electrodes under this voltage excitation is simulated. Figure 4 presents the two-dimensional distributions of streamer morphology at six instants (24.5 ns, 32.5 ns, 36.7 ns, 37.2 ns, 38.2 ns, and 38.7 ns), spanning from streamer initiation to the moment when its head reaches the plate electrode.



(**a**) 24.5 ns (**b**) 32.5 ns (**c**) 36.7 ns (**d**) 37.2 ns (**e**) 38.2 ns (**f**) 38.7 ns

Figure 4. Morphology of the pre-breakdown streamer at different instants.

A clear dynamic process can be observed, in which the streamer gradually forms and propagates forward along the direction of the electric field. Following the application of the pulse voltage, the space charge progressively distorts the initially applied external electric field. During the streamer development, the maximum electric field strength between the electrodes reaches 1.89×10^8 V/m, indicating a strong local field enhancement effect. Based on these observations, the streamer development process can be divided into the following four stages to further elucidate its evolution mechanism.

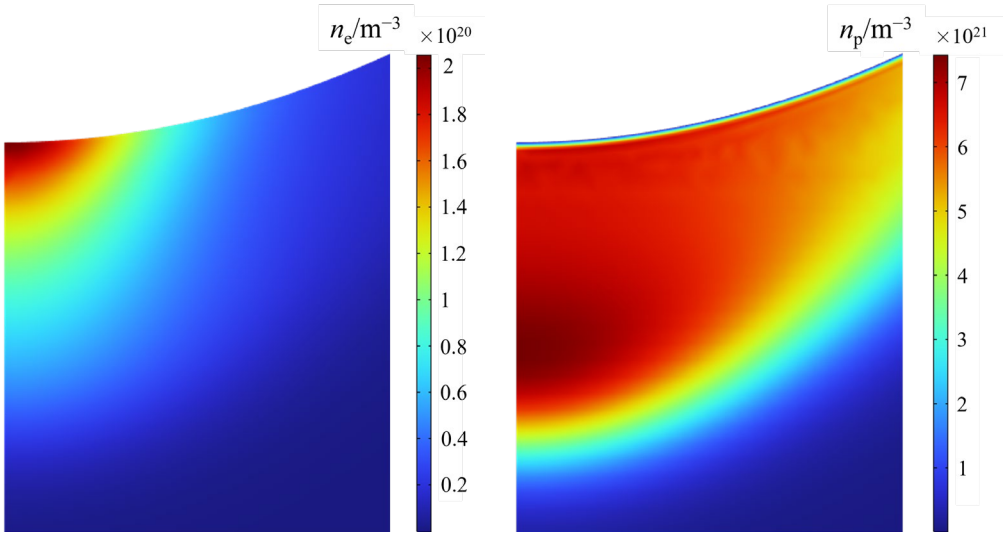
(1) Initiation stage: A localized, spherical electric field concentration zone appears near the needle tip, where the maximum electric field strength has already exceeded the field-induced ionization threshold of water. Under the strong electric field, initial ionization of water molecules occurs near the tip, generating electrons and positive ions, marking the formal onset of the discharge process. However, at this point, the space charge generated by ionization has not yet sufficiently accumulated to form an effective self-consistent distorted field; therefore, no streamer structure with a distinct head and directional extension is observed, and the system remains in the ionization initiation period.

(2) Distortion stage: In this stage, the electric field distribution undergoes significant distortion, and the streamer structure gradually takes shape. The high-field region near the tip transitions from its initial spherical distribution to an axially stretched configuration, exhibiting a pronounced protruding head morphology that indicates the onset of streamer formation, and the peak electric field is reached shortly thereafter. During this stage, the electrons generated by field-induced ionization are rapidly captured by the needle electrode, while the positive ions, having lower mobility, remain and accumulate in the ionization region, forming a net positive space-charge layer, as shown in Figure 5. The electric field produced by this space charge aligns with the direction of the applied field, creating a field superposition and positive feedback effect ahead of the streamer head, which continuously elevates the front-end electric field and promotes forward extension of the ionization region. When the electric field strength and space-charge accumulation together reach a critical condition, the previously diffuse ionization region converges into a streamer head with a well-defined boundary, marking the formal formation of the streamer and the onset of the directional propagation stage.

(3) Propagation stage: The streamer head continues to advance axially toward the plate electrode, and the plasma channel extends accordingly. The head region consistently maintains a high electric field strength and represents the most concentrated region of ionization activity. Owing to the differences in charged-particle mobility, electrons migrate rapidly toward the needle electrode, while positive ions accumulate near the head, resulting in significant space-charge separation. This charge distribution further distorts and enhances the electric field ahead of the head, establishing a self-sustaining ionization propagation mechanism. After the streamer passes, a plasma channel with relatively high electrical conductivity is formed along its path. The high carrier concentration inside the channel provides a low-resistance pathway, significantly reducing the axial electric field strength within the channel and creating a low-field region. The directional extension of the streamer is primarily driven by the high electric field at the head, while the conductivity of the channel body ensures continuous current conduction; together, these two features constitute the typical characteristics of streamer development during the pre-breakdown stage.

(4) Breakdown stage: The streamer head reaches the plate electrode, forming a complete bridging plasma channel. At this point, a relatively uniform low-field channel with axial distribution appears between the needle and plate electrodes, and the axial electric field decreases significantly, marking the end of the pre-breakdown process.

The system is about to transition into the main-discharge stage characterized by high current and concentrated energy release. Meanwhile, the streamer channel radius has fully expanded, indicating that the ionization region has reached a considerable scale before bridging, thereby providing the initial geometric dimensions for the subsequent arc detonation and shock wave formation.



(**a**) Electron number density distribution (**b**) Positive ion number density distribution

Figure 5. Distributions of electrons and positive ions at 32.5 ns.

To assess whether the simulated streamer propagation is physically plausible, the effective average velocity of the streamer front was compared with independent experimental measurements. In the present simulation, the streamer develops from initiation at 24.5 ns to complete bridging of the 2 mm gap at 38.7 ns, giving an effective average propagation velocity of 1.41×10^5 m/s. Šimek et al. [38] reported a propagation velocity of approximately 2.0×10^5 m/s for luminous filaments generated by a positive nanosecond point–plane discharge. Prukner et al. [39], using single-event four-channel ICCD imaging, reported expansion velocities of 1.0×10^5–2.3×10^5 m/s. The simulated velocity is approximately 29.5% lower than the value reported in [38] and lies within the range reported in [39], indicating good agreement in propagation magnitude. The streamer field and radius are reported as model estimates rather than quantities measured under identical conditions. Because the terminal streamer state is subsequently used to initialize the main-discharge model, its influence was further examined by perturbing the terminal state. Varying the channel radius by ±20% changes the deposited energy by −0.41%/+0.34%, the shock-wave energy by −0.68%/+0.55%, the overall efficiency by −0.67%/+0.56% and the pressure at 0.1 m by less than 0.1%, while the peak channel pressure changes by −5.9%/+7.4%. Varying the terminal temperature by ±10% produces no resolvable change because the channel is heated from approximately 10^3 K to above 10^4 K within the first nanosecond. The propagation-speed comparison therefore provides an independent quantitative check of the model, while the terminal-state sensitivity quantifies the uncertainty transferred to the main-discharge calculation.

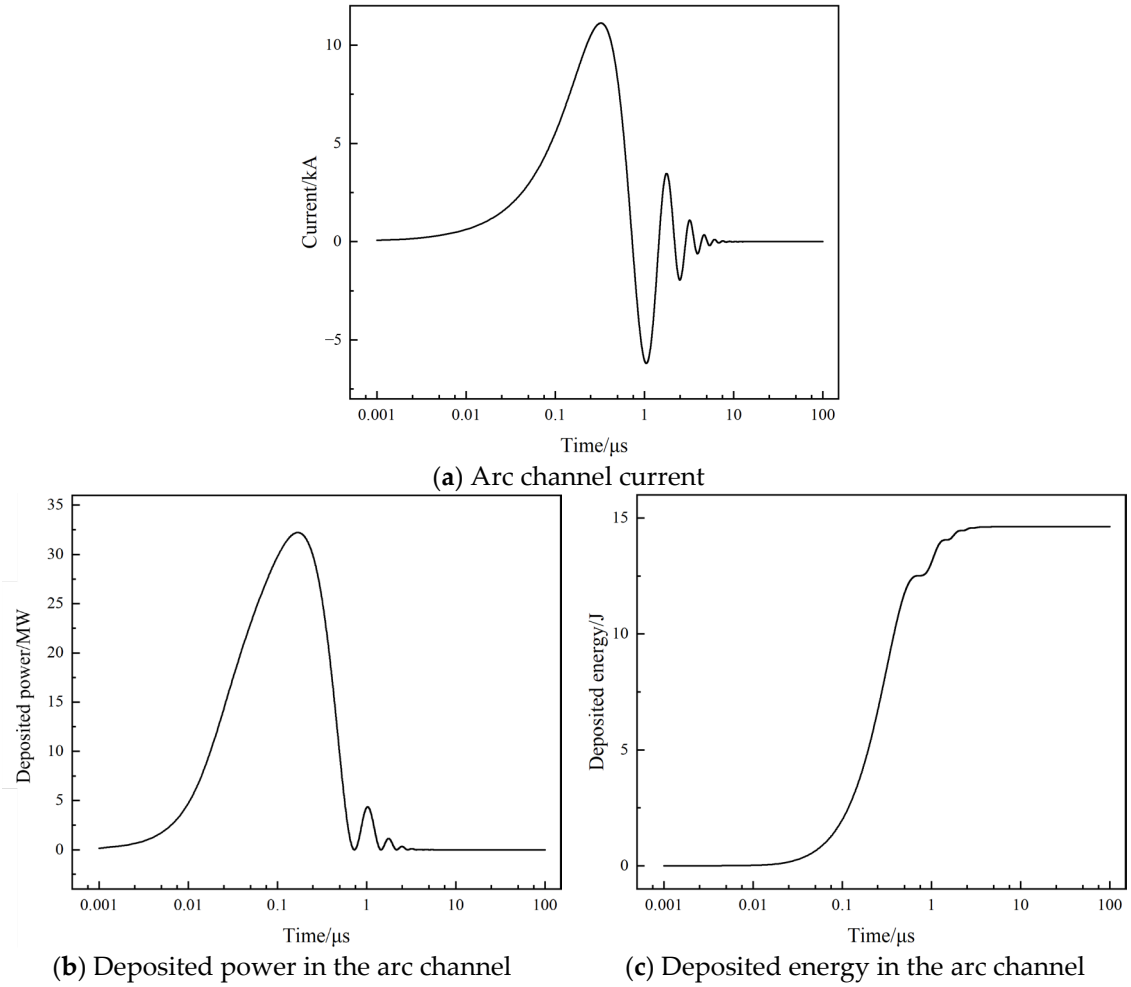
3.2. Main Discharge Process

Following the pre-breakdown simulation results from the preceding section, the morphological parameters of the plasma channel at the end of the pre-breakdown stage—such as radius, length, temperature, and particle density—are taken as the initial conditions and substituted into the arc detonation model for the main discharge stage. In this work, the corresponding model is established in MATLAB R2025a. By solving the

coupled governing equations of this model, the evolution of key physical quantities during the main discharge stage can be obtained, including deposited energy, discharge current, and internal pressure of the channel, thereby enabling a systematic description of the energy conversion and dynamic behavior during this stage.

3.2.1. Arc Channel

In this subsection, the internal evolution characteristics of the arc channel during the period from the onset of the main discharge stage to 100 μs are simulated. Figure 6a presents the temporal evolution of the arc current during this stage. The current exhibits a periodically damped oscillatory behavior, with an oscillation period of approximately 1.5 μs, which remains essentially stable throughout the entire decay process. The peak current reaches 11.1 kA and decays to nearly zero by 10 μs, indicating the termination of the main discharge process. Figure 6b,c show the temporal evolution of the deposited power and deposited energy in the arc channel, respectively. The deposited power also exhibits a damped oscillatory decay, with a peak value of 32.1 MW, dropping to nearly zero after approximately 4 μs; its decay rate is significantly faster than that of the current, and the oscillation frequency is roughly twice that of the current. The deposited energy accumulates rapidly during the initial stage of the discharge, levels off after about 4 μs, and eventually reaches 14.6 J, corresponding to a deposited energy conversion efficiency of approximately 5.4%.



(**a**) Arc channel current

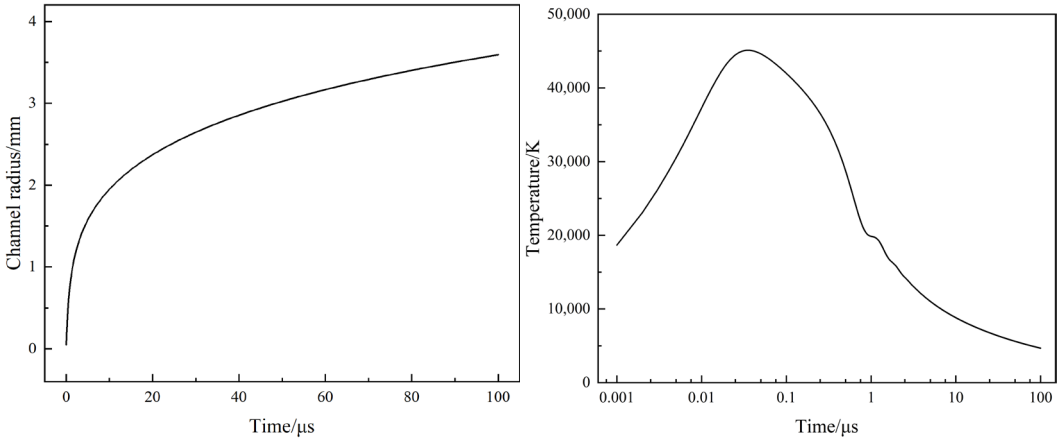
(**b**) Deposited power in the arc channel

(**c**) Deposited energy in the arc channel

Figure 6. Electrical characteristics of the arc channel during the main discharge process.

Figure 7 presents the key physical characteristics of the arc channel during this stage. As shown in Figure 7a, the radius of the arc channel increases rapidly at the initial stage

of the main discharge, after which the growth rate gradually slows and the curve tends to flatten. From Figure 7b, it can be observed that during the early phase of the main discharge, the temperature surges to approximately 45,000 K; subsequently, as the radius growth rate continuously decreases, the temperature rapidly drops below 10,000 K and eventually stabilizes.



(**a**) Arc channel radius (**b**) Arc channel temperature

Figure 7. Physical characteristics of the arc channel.

During the main discharge stage, both the arc current and the deposited power exhibit periodically damped oscillatory decay. However, the deposited power decays at a significantly faster rate, with an oscillation frequency roughly twice that of the current. This is primarily attributed to the rapid increase in channel resistance caused by channel expansion and temperature drop, which leads to energy dissipation over a shorter time scale. The deposited energy stabilizes after approximately 4 μs, with a final conversion efficiency of only 5.4%, indicating that the majority of the stored capacitor energy is not deposited within the arc channel.

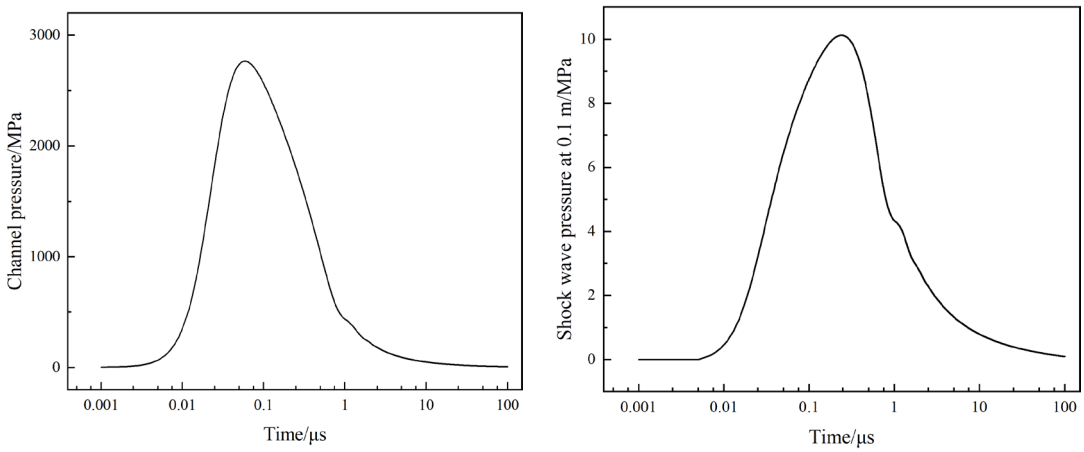
The arc channel radius undergoes an initial rapid expansion, followed by a gradually slower growth and eventual stabilization. The early rapid expansion results from the intense thermal effects induced by the high peak current and deposited power, which raise the channel temperature to tens of thousands of kelvin within an extremely short time. The surrounding water medium at the boundary is violently vaporized and ionized, and the newly generated high-temperature plasma continuously enters the channel, driving its rapid outward expansion. As the deposited power decreases and the temperature drops, the boundary water medium becomes increasingly difficult to vaporize and ionize, and the thermal effects weaken significantly. The primary driving force for channel expansion then shifts to inertial effects, causing the radius growth rate to slow markedly and eventually reach a stable state. At this point, the initial shock wave generation process induced by the rapid channel expansion is essentially completed, and the system subsequently transitions into the stage dominated by bubble pulsation.

3.2.2. Pressure Wave

Figure 8 presents the temporal evolution of the internal pressure of the arc channel and the shock wave pressure after propagation over a distance of 0.1 m during the main discharge stage. At the initial stage of the main discharge, the internal pressure of the arc channel rises sharply with the rapid temperature increase, reaching a peak value of 2765 MPa, and then decreases quickly. In the later stage of the main discharge, the arc channel temperature gradually stabilizes at approximately 4700 K, while the internal pressure of

the channel approaches zero. At a propagation distance of 0.1 m, the peak pressure of the shock wave is 10.1 MPa.

These values are model outputs rather than validated predictions. Their numerical consistency is confirmed by the energy balance: $E_0 = CU_0^2/2 = 272.25$ J, $E_{dep} = 14.630$ J (5.37% of E_0) and $E_{sw} = 7.735$ J (52.87% of E_{dep} and 2.84% of E_0), with the channel energy balance closing to 0 J. Halving the time step from 0.05 ns to 0.025 ns changes the peak current, the deposited energy, the peak channel pressure and the pressure at 0.1 m by less than 0.01%.



(**a**) Internal pressure of the arc channel (**b**) Shock wave pressure at 0.1 m

Figure 8. Shock wave pressure generated during the main discharge stage.

These results present the evolution of the internal pressure of the arc channel during the main discharge stage, which drops sharply from 2765 MPa and eventually approaches zero, as well as the characteristics of the shock wave after propagating to a far distance, where the pressure is significantly attenuated, the waveform is broadened, and only a small portion of the deposited energy is carried by the wave. In the later stage of the main discharge, the channel pressure approaches zero. Although the channel still maintains a relatively high temperature at this point, the external energy injection has essentially ceased, and the significant volume expansion during the channel growth leads to a reduced energy density per unit volume, so that the internal pressure can no longer be sustained.

In the present model, the pressure at a distance r is obtained from Equation (15) by geometric spreading of the channel pressure together with an acoustic time shift. The decrease of the peak pressure with distance therefore arises from two effects: the expansion of the wavefront, represented by the factor a_s/r, and the decay of the channel pressure itself as the channel expands and cools. Viscous and thermal dissipation in the shock front are not resolved in this step, so the calculated pressure at 0.1 m should be regarded as an upper bound for a real dissipative medium.

To ensure the accuracy of the shock wave parameters obtained from the model, the results are compared with typical pulsed discharge shock waves in water. The shock wave waveform obtained in this work is similar to that of measured shock waves from our previous work [37], both exhibiting a steep rising edge on the microsecond scale and a relatively gentle falling edge. The simulated peak pressure and its attenuation trend with propagation distance are also qualitatively consistent with the findings of Chapman [26]. This indicates that the established model is capable of capturing the main characteristics of the shock wave with reasonable fidelity.

3.2.3. Energy Budget

To separate the energy deposited in the channel from the energy carried by the pressure wave, the terms of the channel energy equation were integrated over the solution for the representative operating point (140 kV, 2 mm gap, 0.25 mm tip radius). The resulting budget is given in Table 2.

Table 2. Energy budget at the representative operating point.

Quantity	Symbol	Value (J)	Fraction of E_{dep}	Remark
Capacitor stored energy	E_0	272.25	—	$CU_0^2/2$
Deposited energy in the channel	E_{dep}	14.630	100%	$\int I^2 R_p \, dt$
Increase of channel internal energy	ΔU	5.029	34.4%	$\Delta (wV)$
Mechanical work of channel expansion	W	8.908	60.9%	$\int p \, dV$
Radiative loss at the channel boundary	Q_{rad}	0.693	4.7%	$\int S\sigma_S T^4 \, dt$
Thermal conduction	Q_{cond}	not resolved	—	boundary loss described by Q_{rad}
Shock-wave energy at 0.1 m	E_{sw}	7.735	52.9%	part of W: $4\pi r^2/(\rho_0 c_0)\int p_w^2 \, dt$
Monopole estimate of the shock-wave energy	$E_{sw,mono}$	6.611	45.2%	independent cross-check

$\Delta U + W + Q_{rad} = 14.630$ J $= E_{dep}$, so the channel balance closes to the numerical precision of the integration. The shock-wave energy is not an additional term in this balance; it is the fraction of the expansion work that reaches the observation point at 0.1 m, and its value is lower than W by 1.173 J (13.2% of W) in the equivalent-source representation. Thermal conduction is not resolved separately in the channel energy equation, and viscous dissipation in the shock front is not represented by the propagation model. These limitations are stated so that the budget is not interpreted as a complete partition of all loss mechanisms.

3.3. Influencing Factors of Discharge Development

In this section, the pulse voltage amplitude, electrode gap, and electrode curvature radius are taken as the core variables. The effects of each parameter on the pre-breakdown streamer development and main-discharge energy conversion are investigated through simulations.

3.3.1. Pulse Voltage Amplitude

(1) Streamer Development and Breakdown

Figure 9 presents the morphological characteristics and electric field distributions of the streamer at the moment of breakdown under different pulse voltage amplitudes, where Figure 9a–e correspond to 70 kV, 85 kV, 105 kV, 120 kV, and 140 kV, respectively. It can be clearly observed that as the pulse voltage amplitude increases, the streamer radius gradually enlarges, while the electric field strength at the streamer head gradually decreases. Figure 10 further provides the quantitative variations of streamer radius and breakdown time delay under different voltage amplitudes. The breakdown time delay decreases significantly with increasing voltage amplitude, and the rate of decrease gradually levels off.

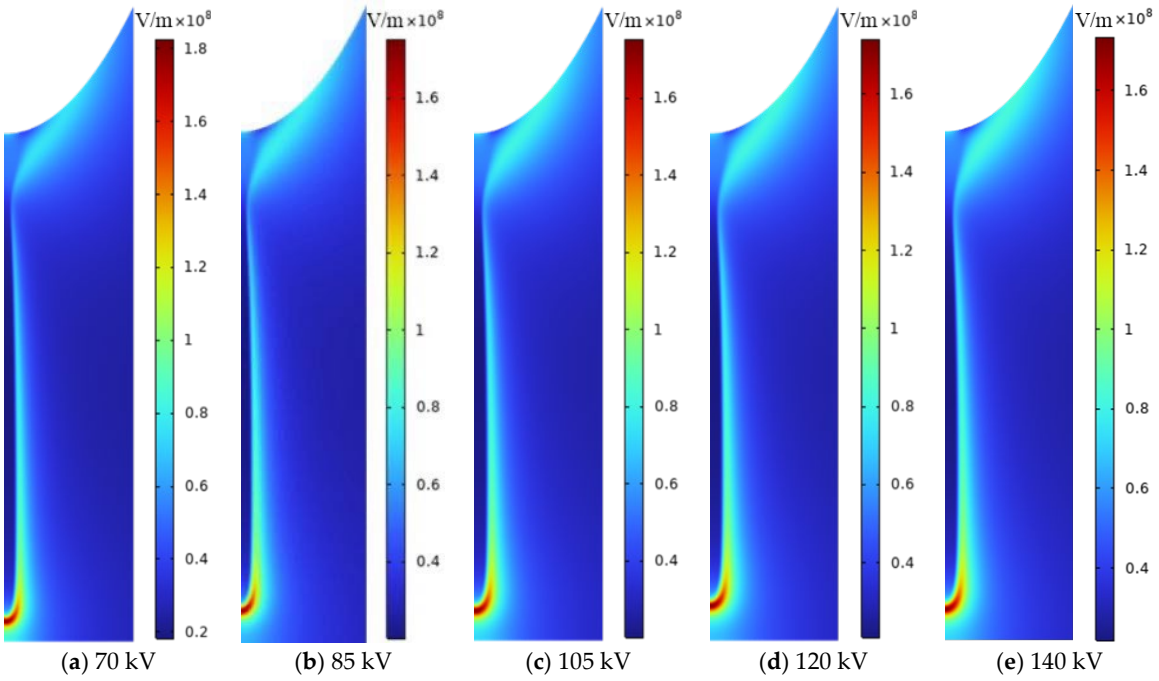


Figure 9. Breakdown spatial electric field distribution at different voltage amplitudes.

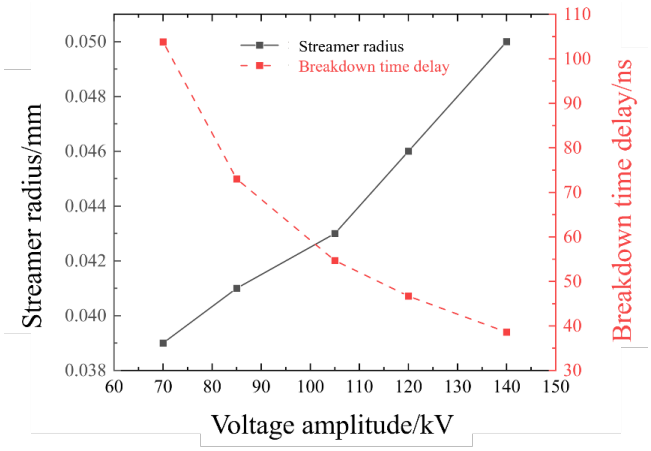


Figure 10. Streamer radius and breakdown time delay at different voltage amplitudes.

Under high voltage amplitudes, the ionization rate increases dramatically, generating a large number of electrons and positive ions. The electrons rapidly migrate toward the needle electrode, while the positive ions, with their lower mobility, remain near the streamer head, forming a broader and denser positive space charge accumulation. This space charge accumulation enhances the electric field behind the head while simultaneously producing a shielding effect on the un-ionized region ahead of the head, thereby flattening the electric field gradient and reducing the peak field strength. At the same time, the increased streamer radius enlarges the geometric curvature radius of the head, weakening the field concentration effect and further contributing to the decrease in peak electric field. The increase in streamer radius results from the higher initial electric field near the needle tip under elevated voltage amplitudes, which significantly enhances ionization reactions in the radial direction. Water molecules are ionized over a wider region, forming a thicker plasma channel. Moreover, the higher voltage amplitude implies more electrical energy input, part of which is consumed in heating and expanding the existing plasma, thereby promoting radial channel expansion. The significant shortening of the breakdown time delay is attributed to the higher energy input into the streamer

under elevated pulse voltages, which accelerates the axial propagation velocity and reduces the time required for the channel to bridge the electrodes.

(2) Energy Conversion in Main Discharge

Figure 11 presents the variation of the shock wave pressure amplitude at a propagation distance of 0.1 m and the proportion of mechanical energy carried by the shock wave relative to the initial stored energy of the capacitor, that is, the overall energy conversion efficiency under different pulse voltage amplitudes. It can be observed that as the pulse voltage amplitude increases, the shock wave pressure amplitude rises, while the overall energy conversion efficiency η exhibits a monotonically decreasing trend.

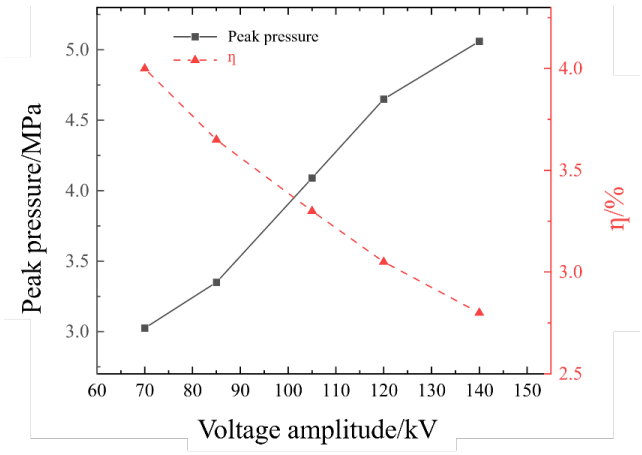


Figure 11. Shock wave peak pressure and overall energy conversion efficiency at different voltage amplitudes.

In this work, the electrical energy entering the plasma channel is defined as the deposited energy, and its proportion in the initial stored energy of the capacitor is defined as the deposited energy conversion efficiency. Meanwhile, the proportion of mechanical energy carried by the shock wave at a propagation distance of 0.1 m relative to the deposited energy is defined as the shock wave energy conversion efficiency. The variations of these two efficiencies with pulse voltage amplitude are shown in Figure 12. The results indicate that the deposited energy conversion efficiency η_B increases with increasing voltage, whereas the shock wave energy conversion efficiency η_E decreases with increasing voltage.

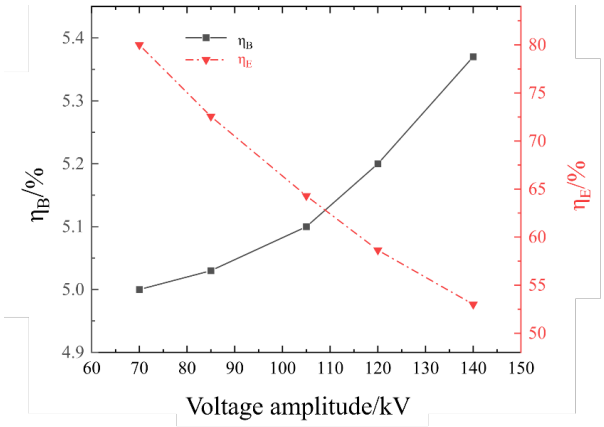


Figure 12. Energy conversion efficiencies at different voltage amplitudes.

The shorter breakdown time delay reduces the energy consumed during the pre-breakdown stage and allows more energy to be injected into the plasma channel during

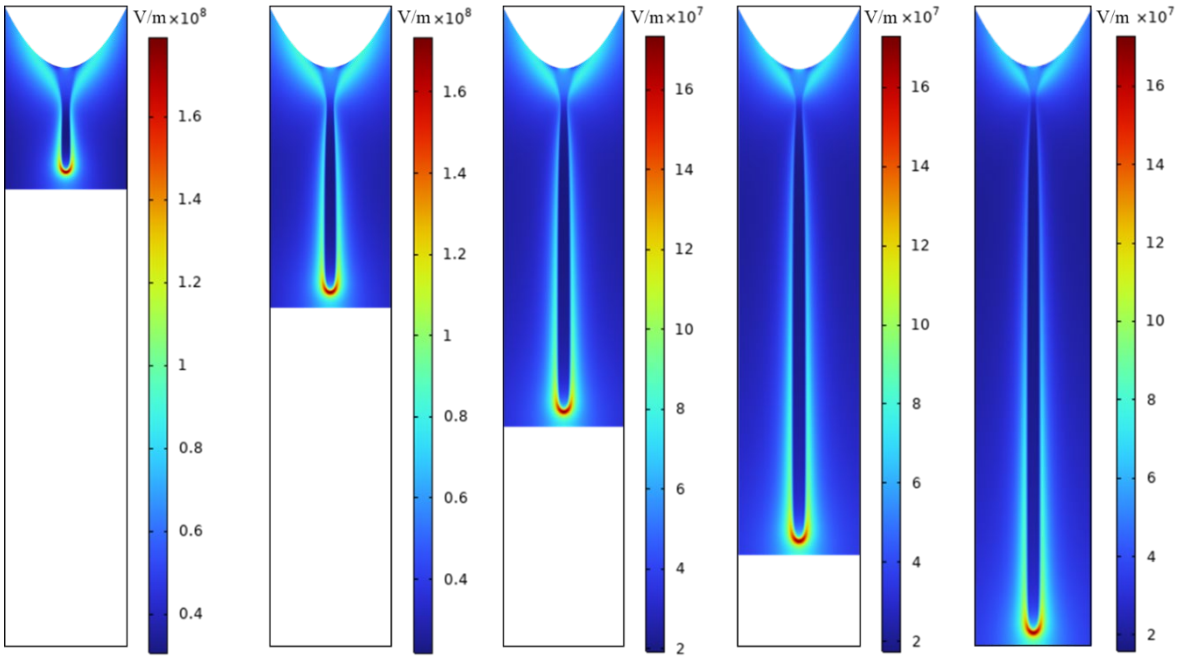
the main discharge stage; consequently, the deposited energy conversion efficiency increases with voltage amplitude. However, under high voltage amplitudes, the energy input power increases, causing the discharge channel temperature to rise sharply. According to the Stefan–Boltzmann law ($P_{rad} \propto T^4$), the radiative heat loss increases exponentially, and a large portion of the deposited energy is dissipated in the form of radiation rather than being converted into mechanical energy of the shock wave. This leads to a decrease in the shock wave energy conversion efficiency with increasing voltage amplitude, which in turn results in the overall energy conversion efficiency exhibiting a monotonically decreasing trend.

3.3.2. Electrode Gap

In this section, the pulse voltage amplitude is fixed at 140 kV, the electrode curvature radius is fixed at 0.25 mm, and the electrode gap is varied as 1 mm, 2 mm, 3 mm, 4 mm, and 5 mm, so as to investigate the effects of the electrode gap on the discharge process in water and the shock wave focusing characteristics.

(1) Streamer Development and Breakdown

The electrode gap not only affects the initiation time of the discharge, but also exerts a significant influence on the subsequent development of the streamer. As shown in Figure 13, Figure 13a–e correspond to gaps from 1 to 5 mm, respectively. With increasing electrode gap, the streamer length at the moment of breakdown increases significantly, and the breakdown time delay also prolongs accordingly. However, the electric field strength at the streamer head at the moment of breakdown does not change appreciably under different gaps, remaining at 1.73×10^8 V/m. Figure 14 shows the streamer radius increases with increasing electrode gap, but the growth rate gradually slows down and exhibits a saturation tendency.



(**a**) 1 mm (**b**) 2 mm (**c**) 3 mm (**d**) 4 mm (**e**) 5 mm

Figure 13. Breakdown spatial electric field distribution at different electrode gaps.

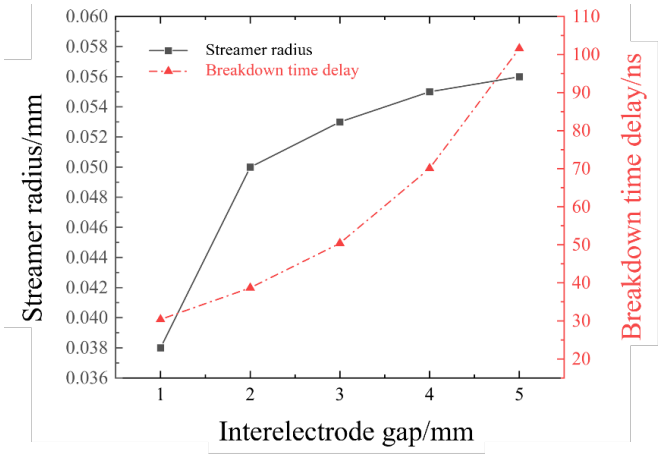


Figure 14. Streamer radius and breakdown time delay at different electrode gaps.

As the electrode gap increases, the breakdown time delay and streamer length both increase. A larger gap means that the streamer must traverse a longer distance; at the same time, the initial electric field strength near the needle tip is reduced, which delays streamer initiation. Moreover, streamer propagation over a longer gap requires additional time, thus the breakdown time delay increases accordingly.

The electric field strength at the streamer head at the moment of breakdown remains approximately 1.73×10^8 V/m under different gaps. This is because the ionization region ahead of the streamer head consistently maintains a critical ionization threshold determined by the dielectric properties of water and the space-charge feedback mechanism, which is independent of the electrode gap. The electrode gap mainly affects the temporal characteristics and geometric scale of the discharge, while exerting only a limited influence on the local ionization intensity at the streamer head.

A larger gap leads to a longer breakdown time delay, allowing more energy to be injected into the streamer channel, and consequently, more energy is allocated to radial expansion, resulting in a larger streamer radius. However, as the gap further increases, the channel length becomes longer, so that the energy density allocated per unit length of the channel decreases, thereby limiting the radial expansion capability. The breakdown time delay shows a sharply increasing trend with the gap, which is not only because the reduced initial electric field at the tip delays initiation, but also because the streamer must overcome stronger dielectric resistance and space-charge shielding effects during propagation over a longer gap, and the propagation velocity attenuates with increasing distance.

(2) Energy Conversion in Main Discharge

Figure 15 presents the variations of the shock wave peak pressure at a propagation distance of 0.1 m and the overall energy conversion efficiency under different electrode gaps. As the electrode gap increases, both the shock wave peak pressure and the overall energy conversion efficiency exhibit a monotonically increasing trend, and the two follow similar patterns: the growth rate is relatively rapid in the smaller-gap range, then gradually slows down and tends toward saturation. The variations of each energy conversion efficiency under different electrode gaps are shown in Figure 16. The deposited energy conversion efficiency exhibits a monotonically increasing trend with increasing electrode gap. However, the variation of the shock wave energy conversion efficiency follows a different pattern, gradually decreasing as the electrode gap increases.

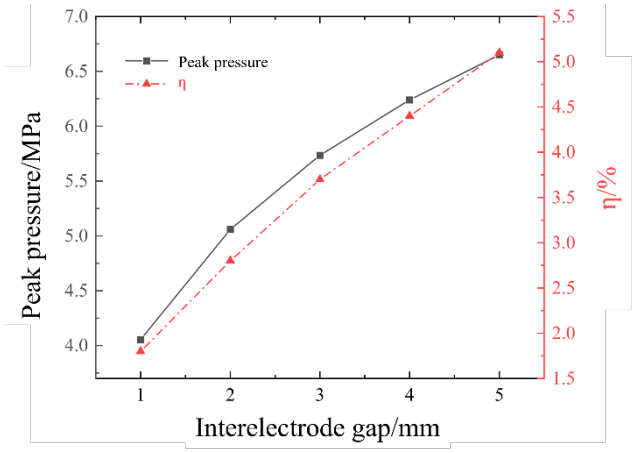


Figure 15. Shock wave peak pressure and overall energy conversion efficiency at different electrode gaps.

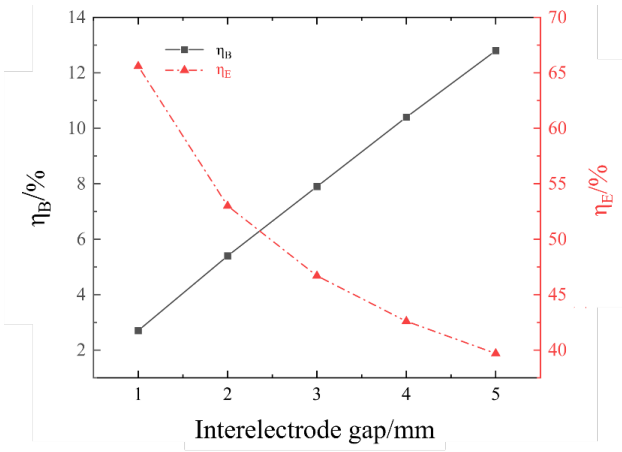


Figure 16. Energy conversion efficiencies at different electrode gaps.

The electrode gap exerts a dual effect on shock wave pressure and energy conversion efficiency: the deposited energy conversion efficiency continues to increase, while the shock wave energy conversion efficiency decreases instead. The superposition of these two opposing trends causes the growth rates of both the overall energy conversion efficiency and the shock wave peak pressure to gradually diminish in the larger-gap range.

The increase in deposited energy conversion efficiency with increasing gap can be attributed to the fact that, although a larger gap prolongs the breakdown time delay and consumes more energy during the pre-breakdown stage, the longer discharge channel leads to an increase in the equivalent resistance of the channel, which in turn promotes greater electrical energy deposition into the plasma channel during the main discharge stage. Within the range of gap distances selected in this work, the energy loss caused by the prolonged breakdown time delay is significantly smaller than the gain in deposited energy resulting from the increased equivalent resistance; hence the deposited energy conversion efficiency continues to rise.

The decrease in shock wave energy conversion efficiency with increasing gap arises mainly from two factors. First, the surface area of the discharge channel increases with the gap, resulting in greater energy dissipation to the surrounding medium through mechanisms such as radiative heat loss and thermal conduction during channel expansion. Second, the increased channel length and prolonged breakdown time delay reduce the temporal concentration of energy release, thereby decreasing the proportion of effective energy available to drive shock wave formation per unit time.

In summary, during the energy deposition stage, a larger gap favors higher conversion efficiency from electrical energy to plasma internal energy; however, in the shock wave formation stage, dissipative mechanisms such as radiative heat loss gradually become dominant, constraining the continuous improvement of mechanical energy conversion efficiency. When the electrode gap is further increased, the sharp decrease in shock wave energy conversion efficiency becomes the dominant factor, offsetting and even surpassing the slowly increasing deposited energy conversion efficiency. The competition and synergy between these two factors cause the peak pressure to increase and then approach saturation, as shown in Figure 17. Within the range of 1–5 mm, the numerical result in this work exhibits a steeply rising trend as the gap increases; whereas in the larger gap range of 10–30 mm, the measured result in our previous work presents a trend of initially rising to a peak at 20 mm before decreasing. Both datasets exhibit a rise followed by saturation, but the comparison cannot establish the quantitative accuracy of the predicted pressure. Measurements under the same gap, voltage, electrode geometry and water conditions are not available in this study, and a matched-condition validation therefore remains an open limitation.

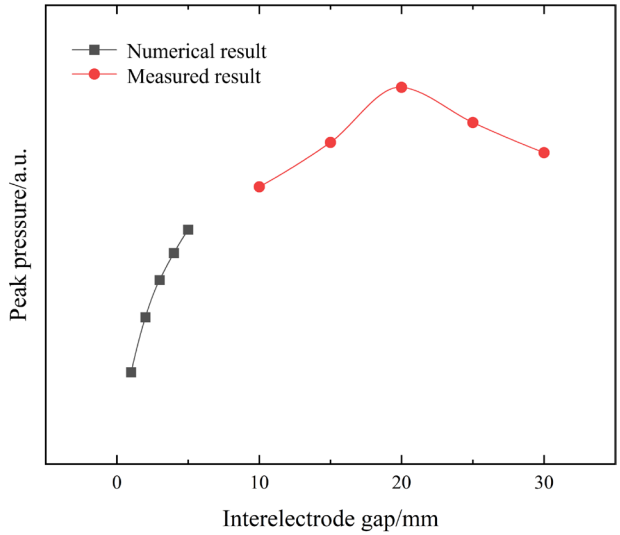


Figure 17. Numerical and measured shock wave peak pressure at different electrode gaps [37].

3.3.3. Electrode Curvature Radius

In this section, the pulse voltage amplitude is fixed at 140 kV, the electrode gap is fixed at 2 mm, and the needle electrode curvature radii are set to 0.1 mm, 0.25 mm, and 0.4 mm, respectively, so as to investigate the effects of the electrode curvature radius on the discharge process in water and the shock wave focusing characteristics.

(1) Streamer Development and Breakdown

The morphological characteristics and electric field distributions of the streamer at the moment of breakdown under different electrode curvature radii are shown in Figure 18, where Figure 18a–c correspond to 0.1 mm, 0.25 mm, and 0.4 mm, respectively, and in Figure 19. As the electrode curvature radius increases, both the breakdown time delay and the streamer radius exhibit an increasing trend, while the electric field strength at the streamer head decreases significantly.

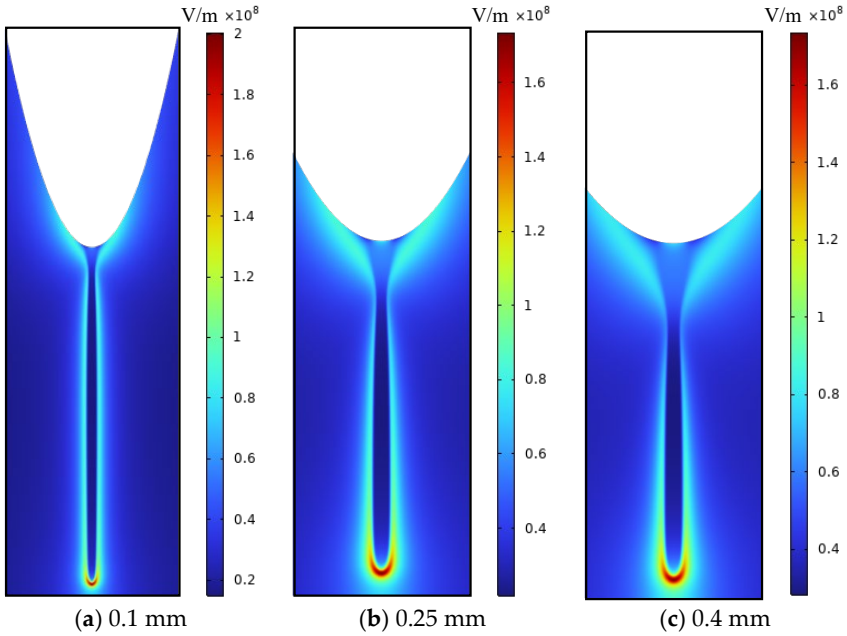


Figure 18. Breakdown spatial electric field distribution at different electrode curvature radii.

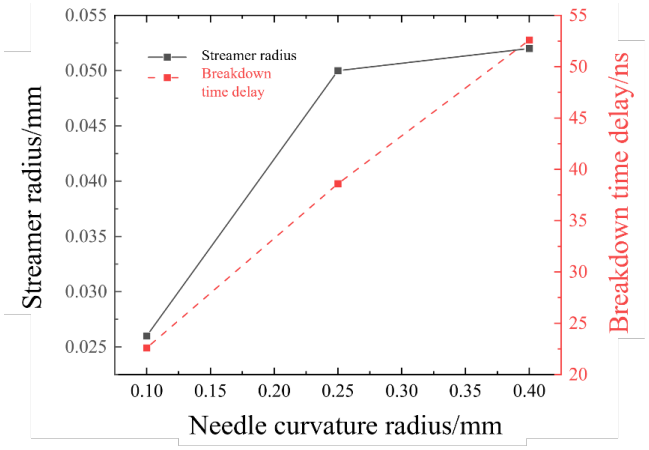


Figure 19. Streamer radius and breakdown time delay at different electrode curvature radii.

The breakdown time delay increases with increasing curvature radius, which originates from the weakening of the field concentration effect at the needle tip. Under a larger curvature radius, the initial electric field strength is reduced, prolonging the time required for water molecules to reach the ionization threshold. At the same time, the decrease in electric field strength at the streamer head weakens the ionization capability and propagation speed ahead of the head, further delaying the streamer bridging process.

The streamer radius increases with increasing curvature radius. This is because the more uniform electric field distribution allows the ionization region to expand in the radial direction, and the reduced electric field at the streamer head weakens the radial constriction effect of the channel.

The electric field strength at the streamer head decreases significantly with increasing curvature radius, which results from the combined effect of geometric effects and space-charge effects. The increase in the streamer head radius weakens the field concentration effect, while the enlarged streamer radius reduces the charge density within the discharge channel, further diminishing the distorted electric field caused by space-charge accumulation. Consequently, the peak electric field at the streamer head at the moment of breakdown decreases markedly with increasing curvature radius.

(2) Energy Conversion in Main Discharge

Figure 20 presents the variations of the shock wave peak pressure at a propagation distance of 0.1 m and the overall energy conversion efficiency under the three electrode curvature radii. It can be observed from the figure that as the electrode curvature radius increases, both the shock wave peak pressure and the energy conversion efficiency exhibit a monotonically increasing trend; however, their growth rates gradually slow down, showing a pronounced saturation effect.

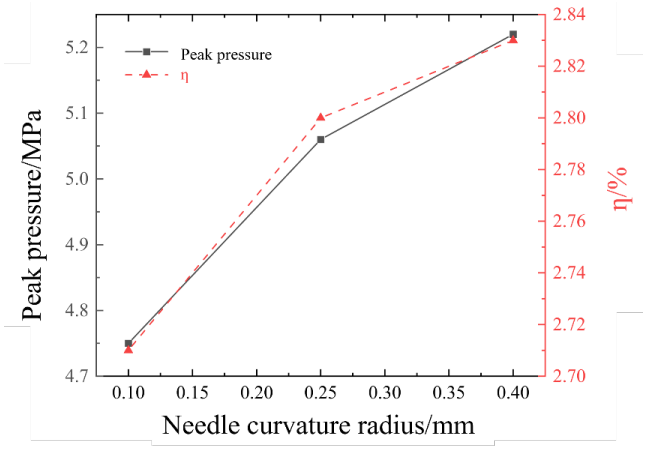


Figure 20. Shock wave peak pressure and overall energy conversion efficiency at different electrode curvature radii.

As shown in Figure 21, both the deposited energy conversion efficiency and the shock wave energy conversion efficiency exhibit an increasing trend with increasing electrode curvature radius. Compared with the case of 0.1 mm, the increases in both energy conversion efficiencies at a curvature radius of 0.4 mm are both approximately 0.2 percentage points, indicating that the improvement is not significant.

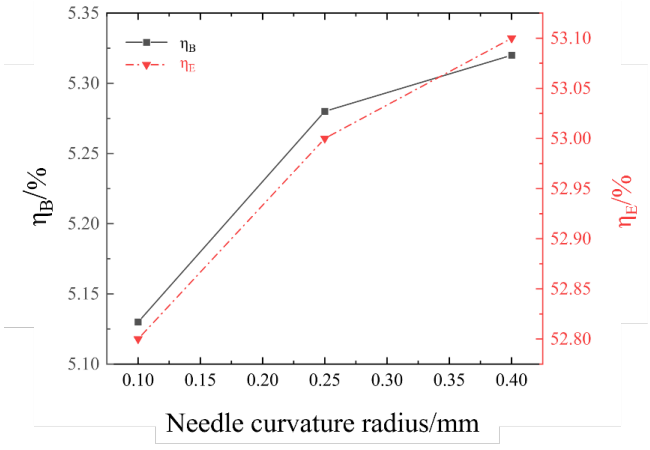


Figure 21. Energy conversion efficiencies at different electrode curvature radii.

As the curvature radius increases, both the shock wave peak pressure and the overall energy conversion efficiency gradually increase, but the growth rate slows down progressively, exhibiting a saturation effect. This variation involves two competing mechanisms. On the one hand, an increase in curvature radius weakens the field concentration effect at the needle tip, delays streamer initiation, prolongs the breakdown time delay, and increases the energy consumed during the pre-breakdown process, reducing the deposited energy conversion efficiency. On the other hand, a larger

curvature radius renders the electrode electric field distribution more uniform and reduces the axial gradient descent, which weakens the electric field gradient near the streamer head and alleviates the inhibition of the vaporization process of the water medium, contributing to an increased energy input power and enhanced energy deposition efficiency during the main discharge process.

Within the selected radius range, the positive effect of electric field homogenization slightly outweighs the negative effect caused by the prolonged breakdown delay, so both the deposited and shock wave energy conversion efficiencies increase overall, albeit with a gradually diminishing growth rate as the two effects approach balance. This local saturation behavior observed in range of 0.1–0.4 mm is consistent with previous experimental results in the comparable interval of 0.25–0.45 mm, where efficiency also rose with increasing radius. However, when the radius was further extended to 0.95 mm in the previous work, the total efficiency peaked at 0.45 mm and then declined significantly, indicating that the global trend is non-monotonic [37]. Thus, the electrode curvature radius exhibits a bidirectional regulatory characteristic: within a relatively small radius, increasing the radius can moderately improve efficiency, but beyond a certain threshold, the positive effect saturates, and further increases contribute even negatively, as confirmed by the observed drop beyond the optimum.

The numerical robustness of the reported trends was checked as follows. Halving the time step from 0.05 ns to 0.025 ns changed the peak current, the deposited energy, the peak channel pressure and the shock-wave energy by less than 0.01%. The pre-breakdown mesh uses 400 divisions along the gap and a maximum element size of 5 μm, which resolves the 2 mm gap and the 0.25 mm tip radius. A systematic mesh-refinement study was not performed and is stated as a limitation of the present work; the fact that the saturation trends are consistent across the three independent parameter sweeps supports their physical rather than numerical origin. To quantify the trends rather than describe them qualitatively, a normalized sensitivity $S = (\Delta Y/Y_0)/(\Delta X/X_0)$ was evaluated over each sweep, as shown in Table 3.

Table 3. Numerical values underlying the parameter studies.

Sweep	U (kV)	d (mm)	r_c (mm)	a_s (mm)	t_d (ns)	p_{peak} (MPa)	η_B (%)	η_E (%)	η (%)
Voltage	70	2	0.25	0.039	105	3.02	5.00	78	4.08
Voltage	85	2	0.25	0.041	72	3.35	5.03	72	3.80
Voltage	105	2	0.25	0.043	55	4.08	5.10	62	3.50
Voltage	120	2	0.25	0.046	47.5	4.65	5.20	57	3.20
Voltage	140	2	0.25	0.050	38.7	5.05	5.36	52	2.78
Gap	140	1	0.25	0.038	30	4.05	2.70	67	1.90
Gap	140	2	0.25	0.050	40	5.05	5.30	52	2.90
Gap	140	3	0.25	0.053	50	5.75	7.90	46	3.70
Gap	140	4	0.25	0.055	70	6.20	10.40	41	4.50
Gap	140	5	0.25	0.056	103	6.65	12.80	39	5.05
Curvature	140	2	0.10	0.026	23	4.75	5.13	52.8	2.71
Curvature	140	2	0.25	0.050	39	5.06	5.28	53.0	2.80
Curvature	140	2	0.40	0.052	52	5.22	5.32	53.1	2.83

The pressures are the values plotted in Figures 11, 15 and 20; for the baseline the pressure at 0.1 m is 10.12 MPa. The breakdown delay is most sensitive to the voltage S = −0.63 (for 70–140 kV), followed by the gap S = 0.61 (for 1–5 mm) and the tip radius S = 0.42 (for 0.1–0.4 mm). The peak pressure is strongly sensitive to the voltage S = 0.67 but much less to the gap S = 0.16 and to the curvature radius S = 0.03. The deposited-energy and

shock-wave energy efficiencies vary in opposite directions in all three sweeps, consistent with the competition between deposited-energy gain and radiative loss described in Sections 3.3.1–3.3.3.

4. Conclusions

This paper has established a numerical simulation system covering the entire process from pre-breakdown to main discharge. Through multiphysics coupling and parametric analyses, the evolution of streamers, energy conversion, and the influence patterns of key parameters have been revealed. The main conclusions are as follows:

A multiphysics coupling model for pre-breakdown based on the field-induced ionization theory has been established, successfully simulating the complete process of streamer initiation to bridging under a needle-plate electrode configuration. Under high-voltage nanosecond pulse excitation, the streamer development can be divided into four stages: initiation, distortion, propagation, and breakdown. The electric field at the streamer head is extremely high, and at the moment of bridging, the channel radius is small while the temperature is relatively high. The charged-particle distributions indicate that the accumulation of positive ions at the streamer head is the primary driving force for field distortion and streamer extension; electrons, owing to their high mobility, are mainly distributed in the middle and rear sections of the channel and migrate toward the anode; negative ions, formed by electron attachment to water molecules, continuously accumulate in the middle and rear sections of the streamer. The axial propagation velocity of the streamer gradually increases, exhibiting a significant accelerating characteristic.

A temperature-dependent arc detonation dynamic model for the main discharge stage has been constructed, describing the energy deposition and shock wave formation processes. The main discharge current exhibits a damped oscillatory characteristic. The deposited energy accounts for only a small portion of the capacitor-stored energy. The initial peak internal pressure of the arc channel is extremely high, followed by a rapid decline owing to reduced energy input and increased volume. During mechanical energy conversion and near-field propagation, the shock wave undergoes significant energy dissipation. After propagating to a certain distance, the peak pressure is greatly attenuated, and the energy carried by the wave constitutes only a fraction of the deposited energy, indicating that the energy carried by the wave is 7.735 J, i.e., 52.9% of the deposited energy. The reduction from the deposited energy to the wave energy is associated with the radiative loss at the channel boundary (4.7% of the deposited energy) and with the difference between the expansion work and the energy carried by the wave (13.2% of the expansion work); thermal conduction and viscous dissipation are not resolved separately in the present model.

The regulatory effects of pulse voltage amplitude, electrode gap, and electrode tip curvature radius on the discharge process and energy conversion have been analyzed. An increase in voltage amplitude shortens the streamer initiation time and breakdown time delay, increases the streamer radius, improves the deposited energy conversion efficiency but reduces the shock wave energy conversion efficiency, resulting in an increased shock wave amplitude but a decreasing trend in overall energy conversion efficiency. An increase in electrode gap delays the streamer initiation time, prolongs the breakdown time delay, increases the streamer radius, continuously improves the deposited energy conversion efficiency, but reduces the shock wave energy conversion efficiency, leading to an increased shock wave amplitude with a decelerating growth rate. An increase in electrode tip curvature radius prolongs the streamer initiation time and breakdown time delay, increases the streamer radius, significantly reduces the head electric field, and slightly improves the energy conversion efficiency but with limited growth. Owing to the competing relationships between deposited energy gain and radiative heat dissipation, as

well as between electric field homogenization and breakdown time delay prolongation, the effects of the above parameters on shock wave amplitude all exhibit saturation behavior.

The integrated pre-breakdown–main-discharge framework developed in this work provides a consistent basis for analyzing how discharge parameters affect energy deposition and shock-wave generation, and for identifying trends that are relevant to the design of underwater pulsed acoustic sources. Its predictions are model-based: they rest on the assumptions stated in Section 2.3. Quantitative prediction of the shock-wave performance of a specific device therefore requires validation against measurements under matched voltage, gap, electrode geometry and water conditions.

Author Contributions: Conceptualization, Y.F., M.Z., Z.M. and B.S.; methodology, H.L., C.L., Q.Y., M.Z. and B.S.; software, K.C. and Z.L.; validation, Y.L. and Z.M.; formal analysis, H.L., M.Z. and Z.L.; investigation, Y.F., J.W. and Z.L.; resources, C.L.; data curation, K.C. and Q.Y.; writing—original draft preparation, J.D.; writing—review and editing, K.C., H.L., J.W. and B.S.; visualization, J.D.; supervision, Y.F., Y.L., J.W., P.W. and B.S.; project administration, C.L.; funding acquisition, P.W. All authors have read and agreed to the published version of the manuscript.

Funding: This work was funded by Fundamental Research Funds (Program No. JTKX24278).

Data Availability Statement: The datasets generated and analyzed during this study are available from the corresponding author upon reasonable request.

Conflicts of Interest: The authors declare no conflict of interest.

References

1. Qiao, L.; Zhang, X.; Yan, B.; Liu, Y. Comparison of Acoustic Signals Produced by Underwater Plasma and Explosive Charge Sound Source. In *Proceedings of the 2020 IEEE 4th Information Technology, Networking, Electronic and Automation Control Conference (ITNEC), Chongqing, China, 12–14 June 2020*; IEEE: Chongqing, China, 2020; pp. 1829–1833.
2. Rehn, K.W.; Riggs, P.K. *Non-Lethal Swimmer Neutralization Study*; Defense Technical Information Center: Fort Belvoir, VA, USA, 2002.
3. Buogo, S.; Plocek, J.; Vokurka, K. Efficiency of Energy Conversion in Underwater Spark Discharges and Associated Bubble Oscillations: Experimental Results. *Acta Acust. United Acust.* **2009**, *95*, 46–59. https://doi.org/10.3813/AAA.918126.
4. Blackmon, F.; Antonelli, L. Experimental Demonstration of Multiple Pulse Nonlinear Optoacoustic Signal Generation and Control. *Appl. Opt.* **2005**, *44*, 103. https://doi.org/10.1364/AO.44.000103.
5. Claverie, A.; Deroy, J.; Boustie, M.; Avrillaud, G.; Chuvatin, A.; Mazanchenko, E.; Demol, G.; Dramane, B. Experimental Characterization of Plasma Formation and Shockwave Propagation Induced by High Power Pulsed Underwater Electrical Discharge. *Rev. Sci. Instrum.* **2014**, *85*, 063701. https://doi.org/10.1063/1.4879715.
6. Stelmashuk, V.; Hoffer, P.; Kolacek, K.; Straus, J. Experimental Study of Spark Channel Expansion in Water. *IEEE Trans. Plasma Sci.* **2020**, *48*, 491–499. https://doi.org/10.1109/TPS.2019.2963536.
7. Prieto, F.E.; Loske, A.M.; Yarger, F.L. An Underwater Shock Wave Research Device. *Rev. Sci. Instrum.* **1991**, *62*, 1849–1854. https://doi.org/10.1063/1.1142527.
8. Gustafsson, G. Experiments on Shock-Wave Focusing in an Elliptical Cavity. *J. Appl. Phys.* **1987**, *61*, 5193–5195. https://doi.org/10.1063/1.338300.
9. Li, X.; Liu, Y.; Tao, L.; Chen, X.; Li, J. Impulse Breakdown of Liquid Water—Influence of Pulse Duration and Gap Distance. *IEEE Trans. Dielect. Electr. Insul.* **2019**, *26*, 1154–1162. https://doi.org/10.1109/TDEI.2019.007918.
10. Jones, H.M.; Kunhardt, E.E. The Influence of Pressure and Conductivity on the Pulsed Breakdown of Water. *IEEE Trans. Dielect. Electr. Insul.* **1994**, *1*, 1016–1025. https://doi.org/10.1109/94.368641.
11. Onsager, L. Deviations from Ohm's Law in Weak Electrolytes. *J. Chem. Phys.* **1934**, *2*, 599–615. https://doi.org/10.1063/1.1749541.
12. Atrazhev, V.M.; Vorob'ev, V.S.; Timoshkin, I.V.; Given, M.J.; MacGregor, S.J. Mechanisms of Impulse Breakdown in Liquid: The Role of Joule Heating and Formation of Gas Cavities. *IEEE Trans. Plasma Sci.* **2010**, *38*, 2644–2651. https://doi.org/10.1109/TPS.2010.2046337.
13. Adda, P.; Lesaint, O.; Boussetta, N.; Vorobiev, E. Vapor Bubble and Streamer Initiation in Water under Long Duration Impulses.

IEEE Trans. Dielect. Electr. Insul. **2018**, *25*, 1967–1973. https://doi.org/10.1109/TDEI.2018.007427.
14. Dobrynin, D.; Seepersad, Y.; Pekker, M.; Shneider, M.; Friedman, G.; Fridman, A. Non-Equilibrium Nanosecond-Pulsed Plasma Generation in the Liquid Phase (Water, PDMS) without Bubbles: Fast Imaging, Spectroscopy and Leader-Type Model. *J. Phys. D Appl. Phys.* **2013**, *46*, 105201. https://doi.org/10.1088/0022-3727/46/10/105201.
15. Aghdam, A.C.; Farouk, T. Multiphysics Simulation of the Initial Stage of Plasma Discharge Formation in Liquids. *Plasma Sources Sci. Technol.* **2020**, *29*, 025011. https://doi.org/10.1088/1361-6595/ab51e3.
16. Halpern, B.; Gomer, R. Field Ionization in Liquids. *J. Chem. Phys.* **1969**, *51*, 1048–1056. https://doi.org/10.1063/1.1672103.
17. Zener, C. A Theory of the Electrical Breakdown of Solid Dielectrics. *Proc. R. Soc. London. Ser. A Contain. Pap. A Math. Phys. Character* **1934**, *145*, 523–529. https://doi.org/10.1098/rspa.1934.0116.
18. Pekker, M.; Shneider, M.N. Initial Stage of Cavitation in Liquids and Its Observation by Rayleigh Scattering. *Fluid Dyn. Res.* **2017**, *49*, 035503. https://doi.org/10.1088/1873-7005/aa6430.
19. Seepersad, Y.; Pekker, M.; Shneider, M.N.; Fridman, A.; Dobrynin, D. Investigation of Positive and Negative Modes of Nanosecond Pulsed Discharge in Water and Electrostriction Model of Initiation. *J. Phys. D Appl. Phys.* **2013**, *46*, 355201. https://doi.org/10.1088/0022-3727/46/35/355201.
20. Shneider, M.; Pekker, M.; Fridman, A. Theoretical Study of the Initial Stage of Sub-Nanosecond Pulsed Breakdown in Liquid Dielectrics. *IEEE Trans. Dielect. Electr. Insul.* **2012**, *19*, 1579–1582. https://doi.org/10.1109/TDEI.2012.6311503.
21. Panov, V.A.; Vasilyak, L.M.; Vetchinin, S.P.; Ya Pecherkin, V.; Son, E.E. Slow 'Thermal' and Fast 'Streamer-Leader' Breakdown Modes in Conductive Water. *J. Phys. D Appl. Phys.* **2018**, *51*, 354003. https://doi.org/10.1088/1361-6463/aad428.
22. Wardlaw, A.B.; Mair, H.U. Spherical Solutions of an Underwater Explosion Bubble. *Shock Vib.* **1998**, *5*, 89–102. https://doi.org/10.1155/1998/690105.
23. Chung, K.-J.; Lee, S.; Hwang, Y.S.; Kim, C.Y. Modeling of Pulsed Spark Discharge in Water and Its Application to Well Cleaning. *Curr. Appl. Phys.* **2015**, *15*, 977–986. https://doi.org/10.1016/j.cap.2015.05.010.
24. Katsuki, S.; Tanaka, K.; Fudamoto, T.; Namihira, T.; Akiyama, H.; Bluhm, H. Shock Waves Due to Pulsed Streamer Discharges in Water. *Jpn. J. Appl. Phys.* **2006**, *45*, 239. https://doi.org/10.1143/JJAP.45.239.
25. Oshita, D.; Hosseini, S.H.R.; Miyamoto, Y.; Mawatari, K.; Akiyama, H. Study of Underwater Shock Waves and Cavitation Bubbles Generated by Pulsed Electric Discharges. *IEEE Trans. Dielect. Electr. Insul.* **2013**, *20*, 1273–1278. https://doi.org/10.1109/TDEI.2013.6571444.
26. Chapman, N.R. Measurement of the Waveform Parameters of Shallow Explosive Charges. *J. Acoust. Soc. Am.* **1985**, *78*, 672–681. https://doi.org/10.1121/1.392436.
27. Lu, X.P.; Zhang, H.H.; Pan, Y.; Liu, K.F.; Liu, M.H. Study on the Pressure Characteristics of Pulsed Discharge in Water. *Explos. Shock Waves* **2001**, *21*, 282. https://doi.org/10.11883/1001-1455(2001)04-0282-5.
28. Martin, J.; Reess, T.; De Ferron, A.; Ruscassie, R.; Rey-bethbeder, F. A New Formula for Predicting the Amplitude of the Dynamic Pressure Wave Resulting from Breakdown in Water Gap. In *Proceedings of the 2014 IEEE International Power Modulator and High Voltage Conference (IPMHVC), Santa Fe, NM, USA, 1–5 June 2014*; IEEE: Santa Fe, NM, USA, 2014; pp. 423–426.
29. Liu, Y.; Li, Z.-Y.; Li, X.-D.; Liu, S.-W.; Zhou, G.-Y.; Lin, F.-C. Intensity Improvement of Shock Waves Induced by Liquid Electrical Discharges. *Phys. Plasmas* **2017**, *24*, 043510. https://doi.org/10.1063/1.4980848.
30. Saito, T.; Marumoto, M.; Yamashita, H.; Hosseini, S.H.R.; Nakagawa, A.; Hirano, T.; Takayama, K. Experimental and Numerical Studies of Underwater Shock Wave Attenuation. *Shock Waves* **2003**, *13*, 139–148. https://doi.org/10.1007/s00193-003-0201-6.
31. Lan, S.; Ding, X.; Wang, J.; Yao, L.; Wang, J. Simulation of the pulsed streamer discharge in water considering the effect of hydrostatic pressure. *Phys. Plasmas* **2024**, *31*, 103902. https://doi.org/10.1063/5.0215425.
32. Qian, J.; Joshi, R.P.; Schamiloglu, E.; Gaudet, J.; Woodworth, J.R.; Lehr, J. Analysis of Polarity Effects in the Electrical Breakdown of Liquids. *J. Phys. D Appl. Phys.* **2006**, *39*, 359–369. https://doi.org/10.1088/0022-3727/39/2/018.
33. Warne, L.; Jorgenson, R.; Lehr, J. *Resistance of a Water Spark*; SAND2005–6994; Sandia National Laboratories: Albuquerque, NM, USA, 2005. https://doi.org/10.2172/876385.
34. Li, X.; Shi, H.; Hu, J.; Wu, J.; Li, X.; Qiu, A. A numerical model for the electrical and shock wave characteristics of underwater pulsed spark discharge. *J. Appl. Phys.* **2024**, *135*, 033302. https://doi.org/10.1063/5.0187919.
35. Kozyrev, A.; Zherlitsyn, A.; Semeniuk, N. Pulsed high-current discharge in water: Adiabatic model of expanding plasma channel and acoustic wave. *Plasma Sci. Technol.* **2022**, *24*, 035402. https://doi.org/10.1088/2058-6272/ac3973.
36. Kratel, A.W.H. *Pulsed Power Discharges in Water*; California Institute of Technology: Pasadena, CA, USA, 2016.
37. Zhang, Y.; Li, B.; Zhang, S.; Zhao, G.; Cao, K.; Song, B. Pressure Characteristics of Underwater High-Voltage Pulsed Discharge Shock Waves Using Needle-Mesh Electrode. *Appl. Sci.* **2026**, *16*, 1361. https://doi.org/10.3390/app16031361.

38. Šimek, M.; Pongrác, B.; Babický, V.; Člupek, M.; Lukeš, P. Luminous Phase of Nanosecond Discharge in Deionized Water: Morphology, Propagation Velocity and Optical Emission. *Plasma Sources Sci. Technol.* **2017**, *26*, 07LT01. https://doi.org/10.1088/1361-6595/aa758d.
39. Prukner, V.; Schmidt, J.; Hoffer, P.; Šimek, M. Demonstration of Dynamics of Nanosecond Discharge in Liquid Water Using Four-Channel Time-Resolved ICCD Microscopy. *Plasma* **2021**, *4*, 183–200. https://doi.org/10.3390/plasma4010011.

Disclaimer/Publisher's Note: The statements, opinions and data contained in all publications are solely those of the individual author(s) and contributor(s) and not of MDPI and/or the editor(s). MDPI and/or the editor(s) disclaim responsibility for any injury to people or property resulting from any ideas, methods, instructions or products referred to in the content.